The Astrophysical Journal, 862:107 (19pp), 2018 August 1 https://doi.org/10.3847/1538-4357/aacb35
© 2018. The American Astronomical Society. All rights reserved.

ASASSN-15nx: A Luminous Type II Supernova with a "Perfect" Linear Decline

Subhash Bose[1,17], Subo Dong[1,17], C. S. Kochanek[2,3], Andrea Pastorello[4], Boaz Katz[5], David Bersier[6], Jennifer E. Andrews[7], J. L. Prieto[8,9], K. Z. Stanek[2,3], B. J. Shappee[10], Nathan Smith[7], Juna Kollmeier[11], Stefano Benetti[4], E. Cappellaro[4], Ping Chen[1], N. Elias-Rosa[4], Peter Milne[7], Antonia Morales-Garoffolo[12], Leonardo Tartaglia[13], L. Tomasella[4], Christopher Bilinski[7], Joseph Brimacombe[14], Stephan Frank[2], T. W.-S. Holoien[11], Charles D. Kilpatrick[15], Seiichiro Kiyota[16], Barry F. Madore[11], and Jeffrey A. Rich[11]

[1] Kavli Institute for Astronomy and Astrophysics, Peking University, Yi He Yuan Road 5, Hai Dian District, Beijing 100871, People's Republic of China
[2] Department of Astronomy, The Ohio State University, 140 W. 18th Avenue, Columbus, OH 43210, USA
[3] Center for Cosmology and AstroParticle Physics (CCAPP), The Ohio State University, 191 W. Woodruff Avenue, Columbus, OH 43210, USA
[4] INAF-Osservatorio Astronomico di Padova, Vicolo dell'Osservatorio 5, I-35122 Padova, Italy
[5] Weizmann Institute of Science, Rehovot, Israel
[6] Astrophysics Research Institute, Liverpool Science Park, 146 Brownlow Hill, Liverpool L3 5RF, UK
[7] Steward Observatory, University of Arizona, Tucson, AZ 85721, USA
[8] Núcleo de Astronomía de la Facultad de Ingeniería y Ciencias, Universidad Diego Portales, Av. Ejército 441, Santiago, Chile
[9] Millennium Institute of Astrophysics, Santiago, Chile
[10] Institute for Astronomy, University of Hawaii, 2680 Woodlawn Drive, Honolulu, HI 96822, USA
[11] Carnegie Observatories, 813 Santa Barbara Street, Pasadena, CA 91101, USA
[12] Department of Applied Physics, University of Cádiz, Campus of Puerto Real, E-11510 Cádiz, Spain
[13] Department of Astronomy and The Oskar Klein Centre, AlbaNova University Center, Stockholm University, SE-106 91 Stockholm, Sweden
[14] Coral Towers Observatory, Cairns, Queensland 4870, Australia
[15] Department of Astronomy and Astrophysics, University of California, Santa Cruz, CA 95064, USA
[16] Variable Stars Observers League in Japan (VSOLJ), 7-1 Kitahatsutomi, Kamagaya 273-0126, Japan
Received 2018 March 31; revised 2018 June 4; accepted 2018 June 5; published 2018 July 27

Abstract

We report a luminous Type II supernova, ASASSN-15nx, with a peak luminosity of $M_V = -20$ mag that is between those of typical core-collapse supernovae and super-luminous supernovae. The post-peak optical light curves show a long, linear decline with a steep slope of 2.5 mag $(100\,\mathrm{day})^{-1}$ (i.e., an exponential decline in flux) through the end of observations at phase $\approx$260 day. In contrast, the light curves of hydrogen-rich supernovae (SNe II-P/L) always show breaks in their light curves at phase $\sim$100 day, before settling onto ^{56}Co radioactive decay tails with a decline rate of about 1 mag $(100\,\mathrm{day})^{-1}$. The spectra of ASASSN-15nx do not exhibit the narrow emission-line features characteristic of Type IIn SNe, which can have a wide variety of light-curve shapes usually attributed to strong interactions with a dense circumstellar medium (CSM). ASASSN-15nx has a number of spectroscopic peculiarities, including a relatively weak and triangular-shaped Hα emission profile with no absorption component. The physical origin of these peculiarities is unclear, but the long and linear post-peak light curve without a break suggests a single dominant powering mechanism. Decay of a large amount of ^{56}Ni ($M_{\mathrm{Ni}} = 1.6 \pm 0.2\ M_\odot$) can power the light curve of ASASSN-15nx, and the steep light-curve slope requires substantial γ-ray escape from the ejecta, which is possible given a low-mass hydrogen envelope for the progenitor. Another possibility is strong CSM interactions powering the light curve, but the CSM needs to be sculpted to produce the unique light-curve shape and avoid producing SN IIn-like narrow emission lines.

Key words: supernovae: general – supernovae: individual (ASASSN-15nx)

1. Introduction

Core-collapse supernovae (CCSNe) are generally believed to originate from the collapse of massive stars with zero age main sequence (ZAMS) masses $M_{\mathrm{ZAMS}} \gtrsim 8M_\odot$. The properties of the resulting transient depend strongly on the mass and composition of the star at death. In particular, Type II supernovae (SNe) represent the broad subclass of CCSNe that have retained a substantial amount of hydrogen envelope at the time of explosion. Their spectra show characteristic prominent hydrogen Balmer lines with P-Cygni profiles, while the other subclasses of CCSNe (Ib and Ic) are characterized by the absence of hydrogen in their spectra.

Traditionally, these hydrogen-rich SNe are classified into two major subclasses, Type II-P and II-L (Barbon et al. 1979; Filippenko 1997), based on their light curve shapes in the photospheric phase. In this classification scheme, the light curve of a SN II-P has a plateau with almost constant brightness for a period of nearly 100 days, whereas the light curve of an SN II-L declines linearly in magnitude after its peak. Various attempts have been made to refine the classifying criteria of these two subclass (see, e.g., Arcavi et al. 2012; Faran et al. 2014). However, with more detections of SNe-II, it has been realized that SN II light curves are too diverse to perfectly divide into "plateau" or "linear" shapes (e.g., Bose et al. 2016; Holoien et al. 2016b; Valenti et al. 2016), and that the distribution of light-curve shapes may be continuous rather than bimodal (Anderson et al. 2014). A continuous distribution of light curve decline rates suggests a continuum in the ejecta parameters controlling the light-curve shape (e.g., the progenitor density profile according to Nakar et al. 2016). Hereafter, we would refer them as a unified subclass: Type II-P/L SNe.

At the end of the photospheric phase, there is a sudden change in the light-curve shape of SN II-P/L to an exponential

[17] Corresponding authors: Subo Dong (dongsubo@pku.edu.cn), Subhash Bose (email@subhashbose.com).

tail with a decline rate typically of about 0.98 mag (100 day)$^{-1}$, which is the rate of energy deposition from the radioactive decay chain of ^{56}Ni → ^{56}Co → ^{56}Fe. Excluding SNe with strong late-time CSM interactions, all common supernovae (CCSNe and SNe Ia) light curves show this nuclear-decay-dominated phase at late times. The rate of energy deposition into the ejecta is governed by the nuclear decay rate, while the light curve shape can be modified based on how the ejecta traps and thermalizes the γ-ray photons released from the nuclear decay. For SNe II-P/L, the ejecta mass is typically large enough to efficiently absorb and thermalize the decay energy, leading to a luminosity decline rate close to the nuclear decay rate. With the end of the recombination-dominated photospheric phase and the onset of the radioactive tail phase, there is a sharp transition in the optical light curve. This transition phase is always seen for all SN II-P/L with well-covered late-time light curves (Anderson et al. 2014).

CCSNe originate from a wide range of progenitors, and their observed properties also show great diversity. The peak absolute magnitude of Type Ib/c and Type II-P/L SNe typically lie within a broad range of $M_V \sim -14$ to -18.5 mag (Li et al. 2011b). In the last decade, we have also seen the emergence of what may be a new class of events: superluminous supernovae (SLSNe) (e.g., Quimby et al. 2007; Smith et al. 2007; Dong et al. 2016; Bose et al. 2018). They are 10–100 times more luminous than typical CCSNe and peak at $M_V < -21$ mag. Their explosion physics and powering mechanisms are not yet understood, though many hypothesize that their progenitors may be stars more massive than those of common CCSNe (Gal-Yam 2012). It is an open question as to whether there is a gap in the SN luminosity function between those of common SNe and the SLSNe (Arcavi et al. 2016); the answer to this question may indicate whether the progenitor masses of SLSNe are just an extension of the normal SNe. Only a few SNe have been discovered with intermediate luminosity (e.g., PTF10iam with $M_{V,\mathrm{peak}} \approx -20$ mag; Arcavi et al. 2016).

Here, we report the latest addition to this rare group of events with luminosities between those of typical CCSNe and SLSNe: ASASSN-15nx. We present the discovery and follow-up observations of this Type II SN to late time, and we find that, unlike any known SN II-P/L, its late-time light curves do not show the transition to a nuclear decay tail.

ASASSN-15nx was discovered (Kiyota et al. 2015; Holoien et al. 2017a) in the galaxy GALEXASC J044353.08-094205.8 (see Figure 1 for an image of the supernova and its host galaxy) on 2016 August 8 during the ongoing All-sky Automated Survey for SuperNovae (ASAS-SN; Shappee et al. 2014), using the quadruple 14 cm "Brutus" telescope at the LCO facility on Haleakala, Hawaii. The ASAS-SN survey regularly scans the entire visible sky for bright supernovae and other extragalactic transients down to $V \sim 17$ mag, and the ASAS-SN discoveries are minimally biased by host galaxy properties (Holoien et al. 2017a). Nearly 100% of the ASAS-SN supernovae also have spectroscopic classifications (Holoien et al. 2017a, 2017b, 2017c). As a result, the ASAS-SN survey provides an unprecedented, spectroscopically complete, host-unbiased sample from an untargeted survey to study supernova statistics. It has also found a range of unusual transients that likely would have been missed in many other surveys (e.g., Dong et al. 2016; Holoien et al. 2016a; Bose et al. 2018). ASASSN-15nx is located at $\alpha = 04^{\mathrm{h}}43^{\mathrm{m}}53\overset{\mathrm{s}}{.}19$ $\delta = -09°42'11\overset{''}{.}22$, which is offset by $0\overset{''}{.}9$ E and $5\overset{''}{.}1$ S from the center of the $z = 0.02823$ (see Section 3; $D_L = 127.5$ Mpc) host galaxy GALEXASC J044353.08-094205.8 (or PGC 987599; $\alpha = 04^{\mathrm{h}}43^{\mathrm{m}}53\overset{\mathrm{s}}{.}13$, $\delta = -09°42'06\overset{''}{.}1$). The offset from the host center is 3.2 kpc.

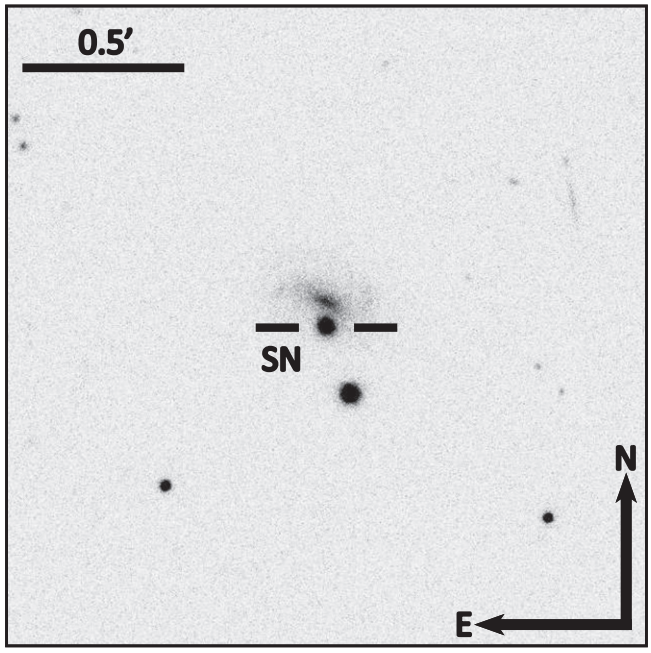


Figure 1. $2' \times 2'$ g'-band image from the 2.6 m Nordic Optical Telescope showing ASASSN-15nx and its host GALEXASC J044353.08-094205.8.

The first detection of ASASSN-15nx was on 2015 July 16.42 UTC (JD 2457219.92). We adopt 2015 July 15.60 (JD 2457219.10 ± 2.00) as the explosion epoch based on fitting the early rising of the light curve with the analytical model from Rabinak & Waxman (2011). We used this as the reference epoch throughout the paper (see Section 3 for further details on the method of constraining the explosion epoch). The object was classified by Elias-Rosa et al. (2015) as a Type II supernova, based on the presence of an Hα emission line. It was further noted that the Hα emission had a peculiar, triangular profile, along with metal lines that appeared to be unusually strong.

We provide brief descriptions of the data collected for ASASSN-15nx in Section 2. We discuss how we estimate explosion epoch, distance, and extinction in Section 3. In Sections 4 and 5, we perform detailed photometric and spectroscopic characterization of the SN. We also identify various peculiarities, which are summarized in Section 6. Finally, in Section 7, we discuss various scenarios that may explain the unique properties of ASASSN-15nx.

2. Data

We initiated multi-band photometric and spectroscopic observations soon after the discovery (+25 day) and continued the observations of ASASSN-15nx until +262 day. Photometric data were obtained from the ASAS-SN quadruple 14 cm "Brutus" telescope, the Las Cumbres Observatory 1.0 m telescope network (Brown et al. 2013), the 1.8 m Copernico, 0.8 m TJO, 2.4 m MDM, 2.6 m NOT, 2.0 m Liverpool telescope, 6.5 m *Magellan* Baade, and 0.6 m Super-Lotis telescopes. The data were obtained in the Johnson–Cousins *BVRI* and SDSS *gri* broadband filters. The images were reduced using standard `IRAF` tasks, and PSF photometry was

performed using the DAOPHOT package. The PSF radius and background extraction region were adjusted according to the FWHM of the image. Photometric calibrations are done using APASS (DR9; Henden et al. 2016) standards available in the field of observation. The *R*- and *I*-band standards were converted from Sloan *gri* magnitudes using the transformation relation given by Lupton et al. (2005). The photometric data of ASASSN-15nx are reported in Table 1.

Medium- to low-resolution spectroscopic observations were made using AFOSC mounted on the 1.8 m Copernico, the Boller & Chivens Spectrograph on the 2.3 m Bok, ALFOSC on the 2.6 m NOT, the Blue Channel spectrograph on the 6.5 m MMT, IMACS and MagE on the 6.5 m *Magellan* Baade telescope, the Boller & Chivens Spectrograph on the 2.5 m Irénée du Pont, and MODS on the LBT with an effective diameter of 11.9 m. All observations were performed in long-slit mode and spectroscopic reductions were done using standard IRAF tasks. The medium-resolution spectra from MODS were reduced using the modsIDL pipeline. The LBT MODS observation on 2016 January 2.20 was also used to estimate the redshift of the host galaxy (see Section 3), with the slit aligned to cross both the host nucleus and the SN. The spectroscopic observations are summarized in Table 2.

3. Explosion Epoch, Distance, and Extinction

The first confirmed detection of ASASSN-15nx was on JD 2457219.92 (2015 July 16.42 UTC), and the last non-detection was about 15 days earlier on JD 2457204.94 with a limiting magnitude of $V = 17.1$ mag. This 15 day gap prevents us from rigorously constraining the explosion epoch directly from observations. However, subsequent observations after the initial detection captured the early rise of the light curve. We modeled these data following Rabinak & Waxman (2011), which is strictly applicable within a couple of weeks after explosion. First, we construct the blackbody SED using the temperature and radius from the Rabinak & Waxman (2011) prescription for a red-supergiant progenitor. The SED is then redshifted and corrected for extinction. The model SED evolution can be represented as

$$F(\lambda, t) = \frac{A \cdot (t - t_0)^{1.62}}{\lambda^5 \left[\exp\left(\frac{B \cdot (t - t_0)^{0.45}}{\lambda}\right) - 1\right]},$$

where t_0 is the explosion epoch, A and B are free parameters, and λ and t have the usual meanings of wavelength and time. The resulting SED evolution is then convolved with the *V*-band filter response to obtain the model light curve. The fit to the early *V*-band observations is shown in Figure 2. Even though the nominal detection significance of the first detection is high, the quality of the image is poor and we exclude it from the model fitting. The data for the subsequent three epochs are cleaner and provide most of the model constraints, leading to an estimated explosion epoch of JD 2457219.10 ± 2.00 (2015 July 15.60 UTC), which is ∼0.8 days prior to our first detection. We adopt this as the reference epoch throughout the paper. The estimated rise time from explosion to *V*-band peak is then ≈22 days.

The host galaxy of ASASSN-15nx does not have any archival redshift or distance estimate. We took a medium-resolution LBT/MODS spectrum with the slit crossing the nucleus of the host

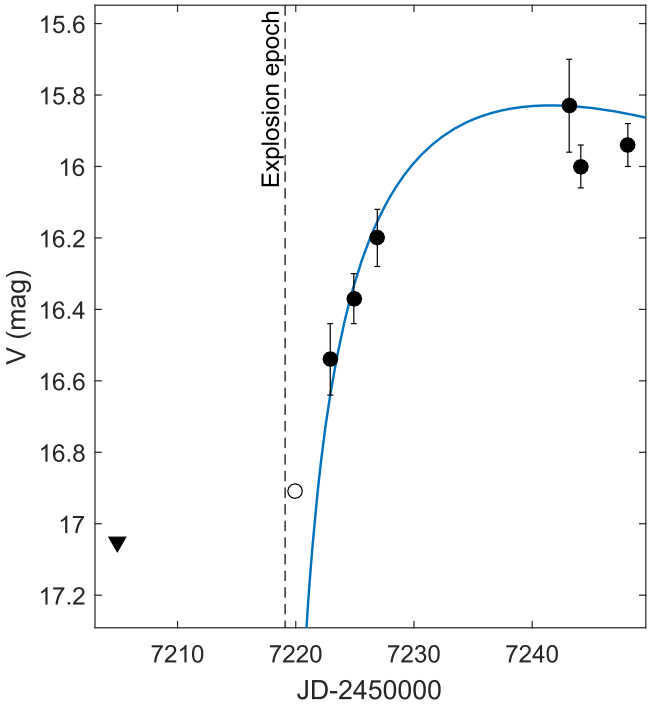


Figure 2. Modeling of the early *V*-band light light curve of ASASSN-15nx, to constrain the explosion epoch. The filled triangle shows the last ASAS-SN non-detection. The open circle represents the first confirmed detection of the SN, but with uncertain photometry. The estimated explosion epoch 0.8 days prior to the first detection is indicated by the dashed line.

galaxy on 165.9 day. The spectrum revealed narrow H I lines (see Figure 3), with Hα being the most prominent feature at 6748.1 Å, corresponding to a host redshift of $z = 0.02823$. The weaker Hβ line was also detected at 4999.4 Å, corresponding to a $z = 0.02840$. These two values are consistent and we adopt $z = 0.02823$ from the strong Hα line. This redshift is also consistent with that inferred from the faint, narrow Hα emission visible on top of the broad Hα P-Cygni profile in four late SN spectra taken between days 166 and 262. The corresponding luminosity distance and distance modulus are $D_L = 127.5 \pm 1.7$ Mpc and DM = 35.53 ± 0.03 mag, assuming a flat cosmology with $H_0 = 67.7$ km s^{-1}Mpc^{-1} and $\Omega_m = 0.308$ (Planck Collaboration et al. 2016).

In the 165.9 day SN spectrum, we detect Galactic Na I D absorption at 5893 Å. We do not detect any Na I D absorption feature at the redshift of the host, which indicates that the host extinction is likely negligible. Therefore, we adopt a total line-of-sight reddening of $E(B - V) = 0.07$ mag (Schlafly & Finkbeiner 2011), entirely due to the Milky Way, which translates into $A_V = 0.22$ mag, assuming $R_V = 3.1$ (Cardelli et al. 1989).

4. Light Curve

4.1. Light Curve Evolution and Comparison

The most unique feature of ASASSN-15nx is its long-lasting, fast-declining linear light curve during the entire phase of evolution following the maximum, as shown in Figure 4. Post-maximum linear decline at a constant rate is observed in all photometric bands, excepting only the *B*-band, which has a steeper slope for ≲50 day. This exceptionally long and nearly "perfectly" continuous linear decline in most optical bands has

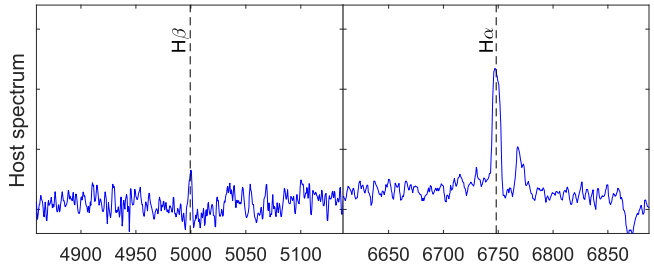


Figure 3. Spectrum for the host nucleus with narrow Hα and Hβ lines at a redshift $z = 0.02823$.

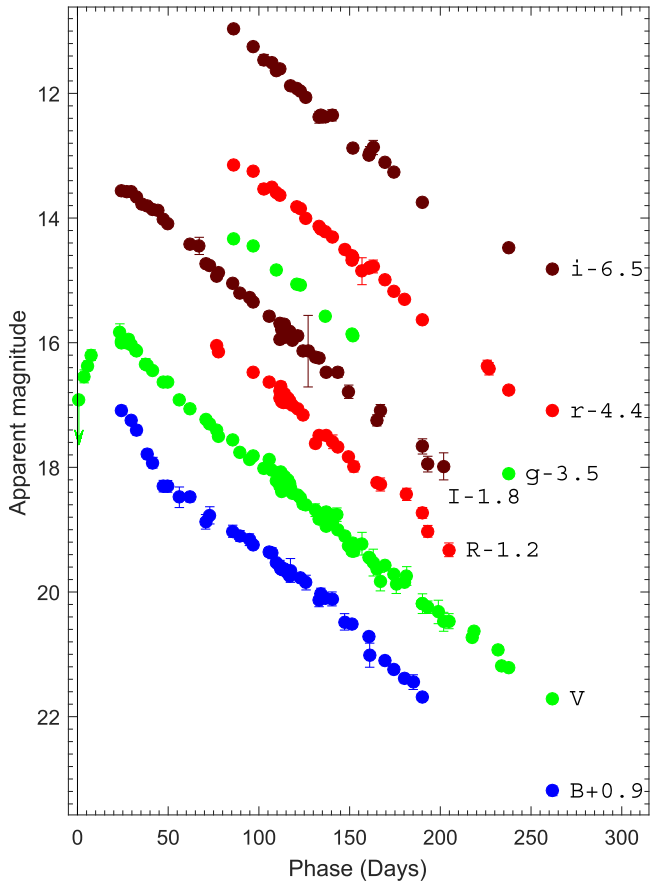


Figure 4. Photometric light curves in the Johnson–Cousins *BVRI* and SDSS *gri* bands. The light curves are vertically shifted for clarity.

not been seen in any other SNe observed to date. The rest-frame light curve decline rates are 2.48 ± 0.03, 2.53 ± 0.08, 2.65 ± 0.04, 2.82 ± 0.25, 2.47 ± 0.10, 2.51 ± 0.09 mag (100 day)$^{-1}$ in the *V, R, I, g, r*, and *i* bands, respectively. The *B* band light curve slope is 5.28 ± 0.28 mag (100 day)$^{-1}$ for <52 day and 2.46 ± 0.07 mag (100 day)$^{-1}$ afterward.

We compare the absolute *V*-band (M_V) light curve of ASASSN-15nx with those for 116 Type II-P/L SNe from Anderson et al. (2014) in Figure 5. The comparison shows that the SN clearly stands out from the sample in terms of both absolute magnitude and the nearly perfect, long linear decline of the light curve. The *V*-band maximum absolute magnitude observed for ASASSN-15nx is −19.92 ± 0.06 mag, making it ∼2.8 mag brighter at +50 day than typical Type II-P/L SNe in the sample.

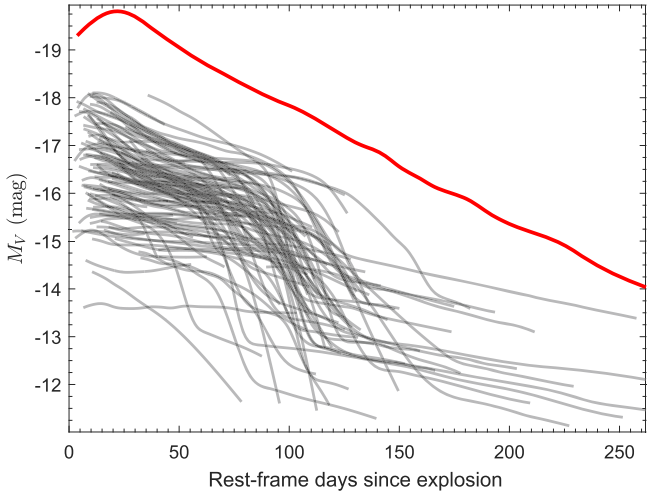


Figure 5. Absolute *V*-band light curve of ASASSN-15nx (red), compared with the sample of Type II SNe presented by Anderson et al. (2014).

We further compare ASASSN-15nx with a sample of well-studied Type II-P/L SNe in Figure 6. The slope of the SN is comparable to the slope during the photospheric phase of SNe 2014G (2.55 mag (100 day)$^{-1}$), 2013by (2.01 mag (100 day)$^{-1}$), and 2000dc (2.56 mag (100 day)$^{-1}$) (Bose et al. 2016), all of which are fast-declining Type II SNe, also known as SNe II-L. All Type II SNe light curves in the comparison sample show distinct photospheric and radioactive tail phases, with a transition near 80–120 days. For qualitative comparison, we also include the absolute *R*-band light curve of PTF10iam (Arcavi et al. 2016) and the *g*-band light curve of ASASSN-15no (Benetti et al. 2018) in Figure 6. PTF10iam had an absolute magnitude similar to ASASSN-15nx (∼−20 mag) and a somewhat slower decline rate of 2.32 mag (100 day)$^{-1}$. PTF10iam is characterized as a luminous and rapidly rising SN II. ASASSN-15nx may have risen equally rapidly, but there is insufficient pre-peak data to be certain. PTF10iam was only observed for ∼90 days, which is a typical timescale for the photospheric phase to have a nearly constant decline rate, so it is not possible to determine whether it had a unique, long-lived linear decline similar to ASASSN-15nx. SN 1979C, SN 1998S, and ASASSN-15no had maximum brightnesses close to, albeit a few tenths of a mag fainter than, that of ASASSN-15nx; they also have late-time light curve decline rates comparable to ASASSN-15nx. However, the light curves of SN 1979C, SN 1998S, and ASASSN-15no show prominent breaks near ∼90 days, so they do not exhibit the most distinguishing feature: the long and continuous linear decline of ASASSN-15nx.

The characteristic radioactive tail phase of normal SNe II ($\gtrsim$150 days), powered by ^{56}Co to ^{56}Fe decay, has a decline slope of ∼0.98 mag (100 day)$^{-1}$ when the γ-ray photons are fully trapped. During this phase, most SNe II in Figure 6 show a decline rate consistent with almost full trapping of the γ-rays. The light curve of ASASSN-15nx is significantly steeper and continued to decline with a constant slope after the early peak. In comparison, the tail of the light curve of the prototypical Type Ia SN 2011fe (Munari et al. 2013), which is also powered by ^{56}Co to ^{56}Fe radioactive decay, has a slope comparable to ASASSN-15nx. The substantially lower γ-ray optical depth in SNe Ia increases the fraction of escaping γ-ray photons and makes the light curve steeper than typical SNe II. The similarity in light

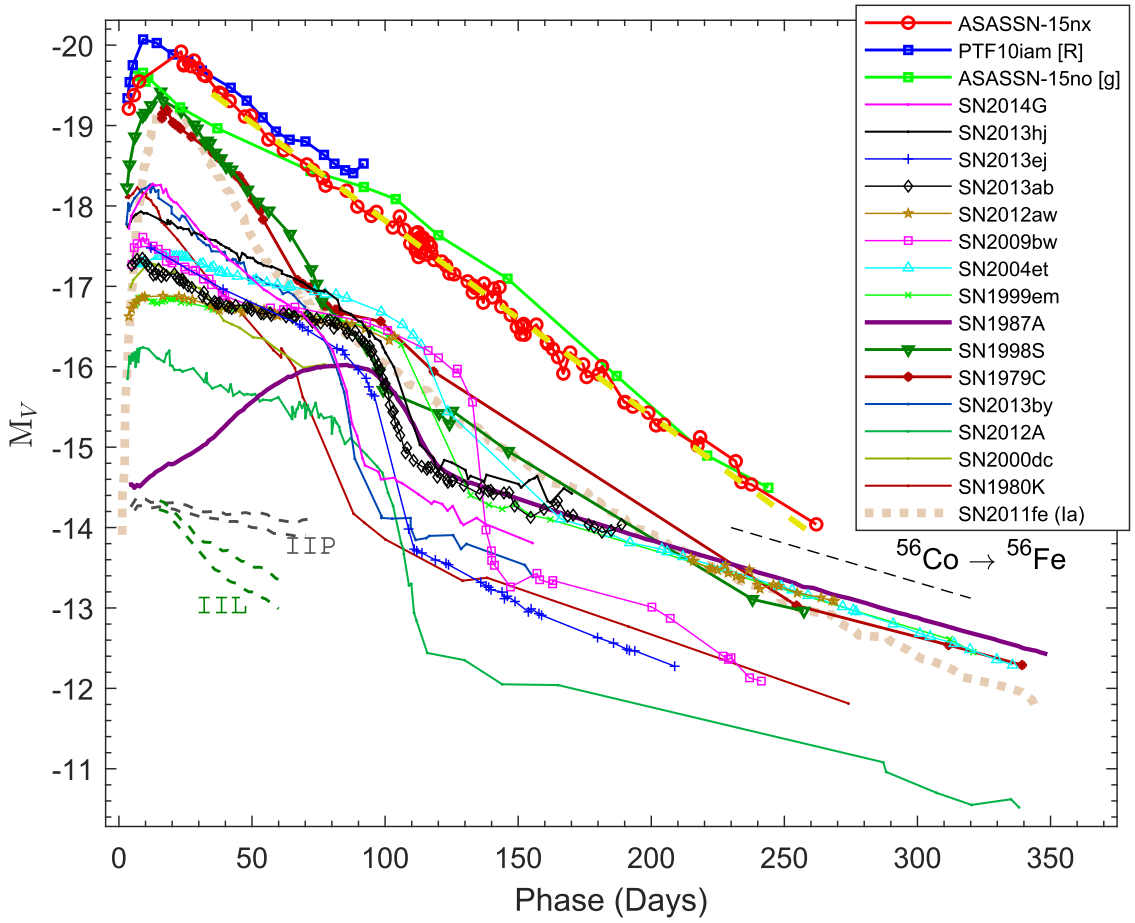


Figure 6. Absolute *V*-band light curve of ASASSN-15nx, as compared to other Type II SNe and the Type Ia SN 2011fe. The exponential decline of a light curve following the radioactive decay law for ^{56}Co → ^{56}Fe is shown with a black dashed line. A best-fit straight line (yellow dashed) is shown on top of the ASASSN-15nx light curve, to emphasize the linearity of decline. On the bottom left side, pairs of dashed lines in gray and green represent the slope range for the Type II-P and II-L SNe templates, as given by Faran et al. (2014). The adopted explosion time in JD-2400,000, distance in Mpc, $E(B-V)$ in mag, and the references for observed *V*-band magnitude, respectively, are : SN 1979C—43970.5, 16.0, 0.31; Barbon et al. (1982b), de Vaucouleurs et al. (1981); SN 1980K—44540.5, 5.5, 0.30; Barbon et al. (1982a), NED database; SN 1987A—46849.8, 0.05, 0.16; Hamuy & Suntzeff (1990); SN 1999em—51475.6, 11.7, 0.10; Leonard et al. (2002); Elmhamdi et al. (2003); SN 2000dc—51762.4, 49.0, 0.07; Faran et al. (2014), NED database; SN 2004et—53270.5, 5.4, 0.41; Sahu et al. (2006); SN 2009bw—54916.5, 20.2, 0.31; Inserra et al. (2012); SN 2012A—55933.5, 9.8, 0.04; Tomasella et al. (2013); SN 2012aw—56002.6, 9.9, 0.07; Bose et al. (2013); SN 2013ab—56340.0, 24.0, 0.04; Bose et al. (2015b); SN 2013by—56404.0, 14.8, 0.19; Valenti et al. (2015); SN 2013ej—56497.3, 9.6, 0.06; Bose et al. (2015a); SN 2013hj—56637.0, 28.2, 0.10; Bose et al. (2016); SN 2014G— 56669.7, 24.4, 0.25; Bose et al. (2016); PTF10iam— 55342.7, 453.35, 0.19; Arcavi et al. (2016); SN 2011fe—55797.2, 6.79, 0.023; Munari et al. (2013); ASASSN-15no—57235.5,153.5, 0.045; Benetti et al. (2018).

curve shapes between SNe Ia and luminous SNe IIL, such as SN1979C, has been discussed before (Doggett & Branch 1985; Wheeler et al. 1987; Young & Branch 1989), pointing to the possibility that luminous SN IIL might also be powered by the decay of a large amount of ^{56}Ni, like SNe Ia. We explore this possibility for ASASSN-15nx in Sections 4.2 and 7.1.

In Figure 7, we present the extinction-corrected $(B-V)_0$ and $(V-I)_0$ color evolution of ASASSN-15nx, as compared with several SNe IIP/L and the Type IIL/n SN 1998S. For ASASSN-15nx, the magnitudes are loosely interpolated to match corresponding photometric epochs for each pair of bands; this also serves to reduce the random fluctuations from internal uncertainties in the photometry. For $t < 50$ day, ASASSN-15nx continues to become redder, following a trend similar to other SNe II. After +50 day, however, ASASSN-15nx shows very little change in color, with mean values $(B-V)_0 = 0.450 \pm 0.016$ and $(V-I)_0 = 0.598 \pm 0.009$ mag. By contrast, a typical SNe IIP/L continues to evolve to substantially redder colors. However, SN IIL/n SN 1998S shows a color evolution similar to ASASSN-15nx in terms of the mean colors and the absence of evolution after ∼60 days.

We fit blackbody models to the extinction-corrected *B*-, *V*- and *I*-band magnitudes. Figure 8 shows the resulting evolution of the effective temperature and radius. The radius initially increases until +50 days, where the photospheric phase ends and the ejecta becomes optically thin. During this phase, the temperature shows a steady decline as the ejecta cools down with expansion. The best-fit effective temperature then starts to rise until ∼135 days, before again beginning a slow decline. This blackbody temperature evolution is unlike that of normal SNe, where usually we simply see monotonic declines (e.g., Bose et al. 2013, 2015b).

4.2. Bolometric Light Curve and ^{56}Ni Mass

In Figure 9, we compare the pseudo-bolometric (3335–8750 Å) light curves of ASASSN-15nx to a sample of well-studied SNe II. The pseudo-bolometric luminosities for all SNe in the sample are constructed following the method described in Bose et al. (2013).

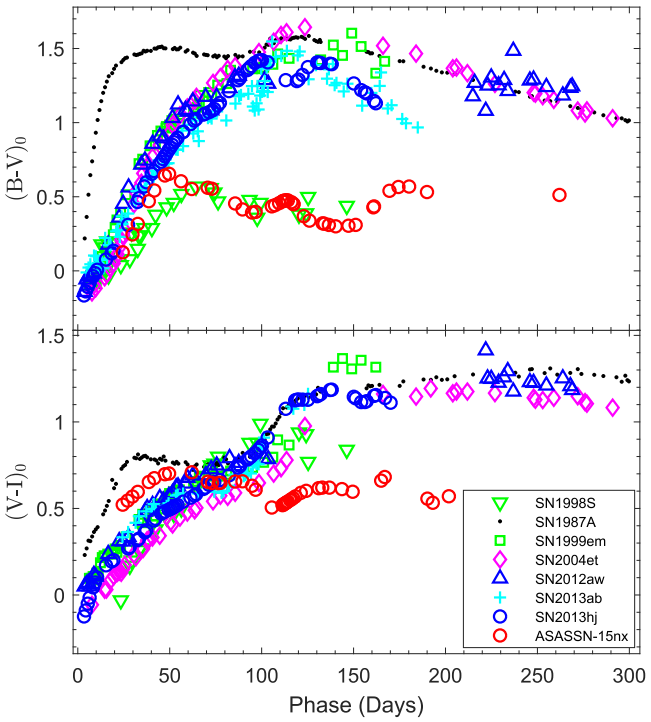


Figure 7. Color evolution of ASASSN-15nx, as compared to the well-studied Type II SNe 1987A, 1999em, 2004et, 2012aw, 2013ab, and 2014hj, and also the Type IIL/n SN 1998S. The references for the data are same as in Figure 6.

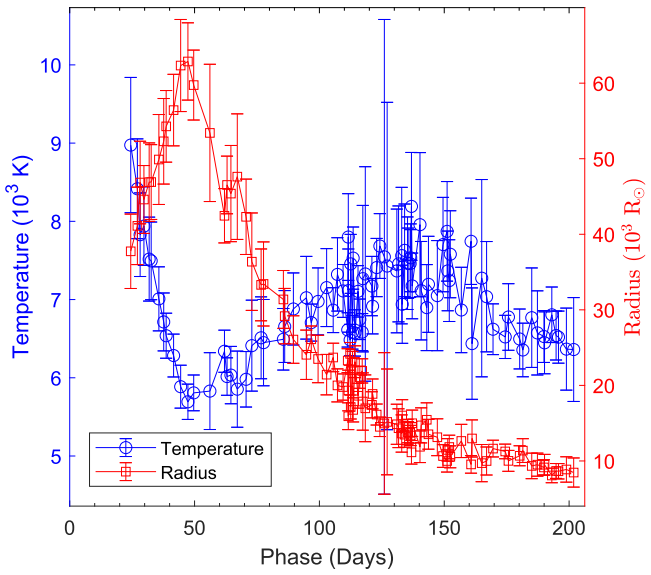


Figure 8. Temporal evolution of the blackbody temperature (blue, left scale) and radius (red, right scale) of ASASSN-15nx.

The light curve decline rate for ASASSN-15nx is 1.05 dex $(100\,\mathrm{day})^{-1}$, which is ∼3 times faster than that expected for a light curve powered by the radioactive decay of ^{56}Co to ^{56}Fe.

Next, we modeled the blackbody bolometric luminosity, using a pure radioactive ^{56}Ni → ^{56}Co → ^{56}Fe decay model. The two free model parameters are the ^{56}Ni mass $M_{\rm Ni}$ and the γ-ray trapping parameter $t_{0\gamma}$, which defines the evolution of the γ-ray optical depth as $\tau_g \sim t_{0\gamma}^2/t^2$. While all the positron kinetic energy from ^{56}Co decay is trapped, only $[1 - \exp(-t_{0\gamma}^2/t^2)]$ fraction of

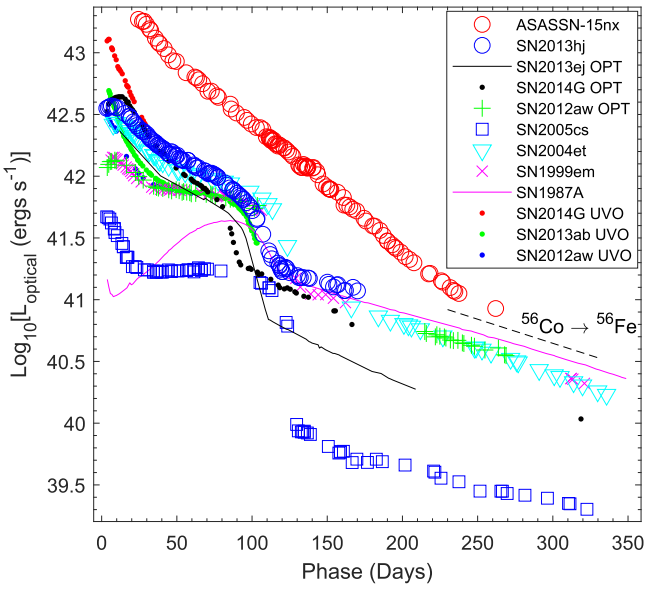


Figure 9. *UBVRI* pseudo-bolometric light-curve of ASASSN-15nx, as compared to other well-studied SNe. Light curves, including UV contributions, are also shown for SNe 2012aw, 2013ab, and 2014G (labeled as UVO). The adopted distances, reddenings, and explosion times are the same as in Figure 6. The slope of a light curve powered by the radioactive decay of ^{56}Co → ^{56}Fe is shown with the dashed line.

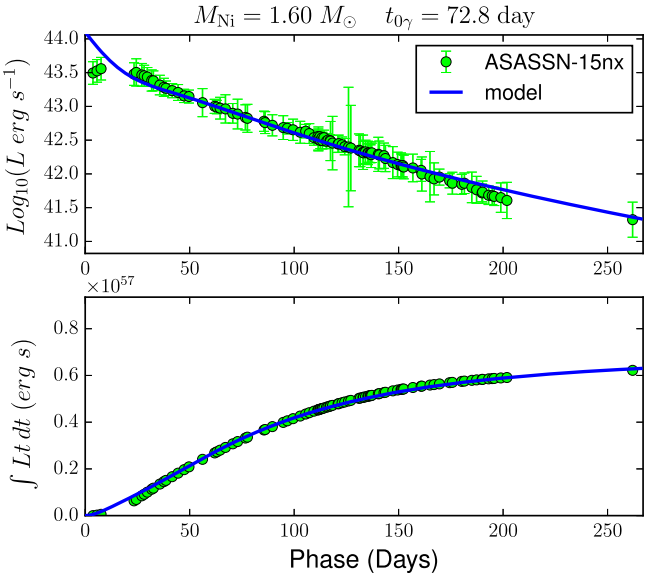


Figure 10. Radioactive decay models of the bolometric light curve (top panel) and the time-weighted integrated radiated energy (bottom panel) of ASASSN-15nx.

the γ-ray decay energy is trapped in the envelope (see the discussions of this approximation in, e.g., Clocchiatti & Wheeler 1997; Chatzopoulos et al. 2012). As shown in the top panel of Figure 10, we find a reasonable fit for $M_{\rm Ni} = 1.6 \pm 0.2\ M_\odot$ and a γ-ray trapping factor $t_{0\gamma} = 73 \pm 7$ days. Although the overall light curve is matched well by the model, there are some noticeable deviations at both early (<25 days) and late (∼200 days) times. Even if the light curve is entirely powered by the radioactive decay, this simple model is not expected to fully capture the light-curve evolution at early phases when the ejecta is optically thick and diffusion is important. The deviation at late time might reflect

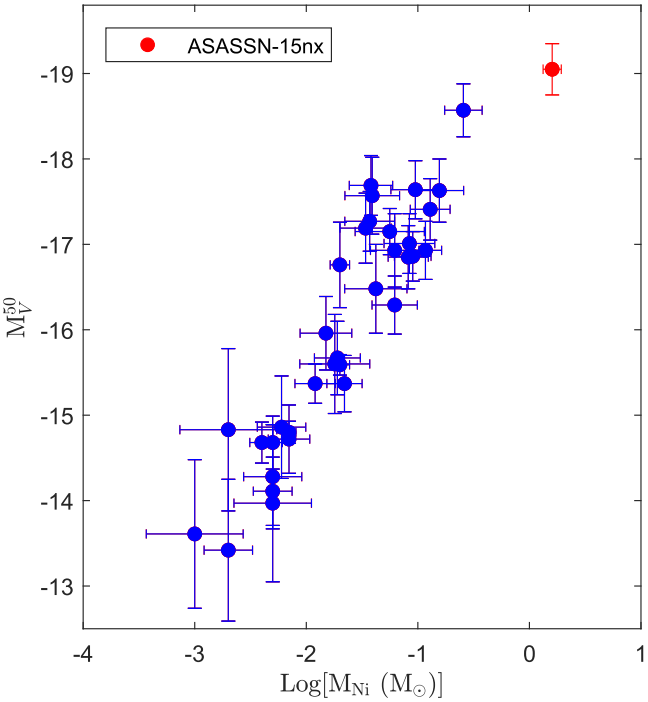


Figure 11. Absolute V-band magnitude at $t = 50$ days as a function of the estimated ^{56}Ni mass for the SNe II sample, from Hamuy (2003) and Spiro et al. (2014). ASASSN-15nx, shown with a red dot, lies on the extrapolation of the correlation to higher masses and luminosities.

inaccuracies in either the physical assumptions of the simple radioactive decay model or the blackbody model used in deriving the bolometric light curve.

To gain more insight into the powering source, we also used the time-weighted integrated luminosity method to model the light curve (Katz et al. 2013; Nakar et al. 2016; Wygoda et al. 2017). The results are shown in the bottom panel of Figure 10. By comparing time-weighted integrated luminosity with a radioactive decay model during the post-photospheric phase, we can verify the powering source of the entire light curve. Katz et al. 2013 showed that the time-weighted integrated luminosity ($\int_0^t L(t')t'dt'$) can also be used to put an additional constraint on the ^{56}Ni mass during the post-photospheric phase—provided the light curve is solely powered by radioactive decay, as in SNe Ia. For this purpose, early time estimates of the luminosity are required, so we extrapolated the temperature into the pre-peak phases and scaled the SED to the V-band flux at fixed temperature. The blackbody luminosity is listed in Table 3. The uncertainty introduced by the extrapolation will eventually become smaller, at larger values of t, due to the time weighting of the integral. The comparison of the integrated time-weighted luminosity shows that the total energy budget of ASASSN-15nx is consistent with almost fully radioactive decay energy, which raises the possibility that it is the dominant powering source of the light curve.

In Figure 11, we show the correlation between the ^{56}Ni mass and the V-band luminosity M_V^{50} at $t = 50$ days for the 34 Type II SNe from Hamuy (2003) and Spiro et al. (2014), along with ASASSN-15nx. As one would expect, ^{56}Ni mass increases with luminosity, but with considerable scatter in the correlation (see Pejcha & Prieto 2015). ASASSN-15nx is consistent with an extrapolation of this correlation, while it clearly stands out at the higher extreme end of the luminosity distributions.

The blackbody model may not always be a good approximation, especially in the optical thin phases. We also constructed the bolometric light curve using bolometric corrections derived empirically from other well-observed Type II SNe. The correction factor is calibrated as a function of broadband color. We adopt the bolometric correction from Bersten & Hamuy (2009) based on the $(B - V)$ color. Because B-band data are not available during the pre-peak phases, the $(B - V)$ color is linearly extrapolated from the color curve for $t < 50$ days. By modeling this bolometric light curve, we estimate $M_{Ni} = 1.3 \pm 0.2\ M_\odot$ and $t_{0\gamma} = 71 \pm 10$ days. This value of nickel mass is consistently within ~20% of that estimated with our earlier model, and the γ-ray trapping factor is also similar. We caution that the bolometric luminosities used in this method may also be inaccurate for an SN like ASASSN-15nx, whose light curve, color, and spectroscopic evolution are significantly different from generic SNe II.

5. Optical Spectra

5.1. Key Spectral Features

The spectroscopic evolution of ASASSN-15nx from $t = 53$ to 262 days is presented in Figure 12. One striking feature is the Hα emission profile, which has an unusual triangular shape in the earliest spectra at $t = 53$ days. We further discuss the Hα profile and its evolution in Sections 5.2 and 5.3. Forbidden [Ca II] ($\lambda\lambda$ 7291, 7324) emission, which usually is not visible until the early nebular phase ($\gtrsim$120 days), can be seen throughout our observing campaign. The Ca II multiplets ($\lambda\lambda$ 8498, 8542, and 8662) are not detected at $t = 53.3$ days, though the SNR in the relevant part of the spectrum is relatively low, while they are clearly visible at $t = 87.4$ days, which is typical of SNe IIP/L. O I emission near 7780 Å is another prominent feature in the 53 day spectra and is present throughout the spectral evolution. The strong O I emission feature appears unusually early for a Type II SN. Interestingly, the O I line has a doubly peaked profile in the 53 day spectra, which evolves into a singly peaked profile by 96.7 days and is no longer present in all subsequent spectra. The origin of the redder component of the double-peaked profile is not clear (as indicated by a question mark in Figure 12). The overall spectral appearance and the early presence of [Ca II] and strong O I features at day 53 make the spectrum appear much more evolved than typical SNe IIP/L at a similar phase. Another noticeable feature in all the spectra is the apparent continuum break near 5500 Å. The continuum level on the bluer side is about 25% higher than on the red side (see further discussions in the context of SYNOW modeling below and also in Section 7.2). The evolution of the prominent metallic lines of Fe II ($\lambda\lambda$ 4924, 5018, 5169) and Na I D (5893 Å) is typical of SNe II.

We used SYNOW[18] (Fisher et al. 1997, 1999; Branch et al. 2002) to model the spectra and identify features. In order to mimic the continuum break, we multiply the model spectrum with a Gaussian convolved step function whose amplitude and width are tuned to fit the observed spectrum. This modifier function is shown in the top panel of Figure 13, where the blue continuum beyond 5500 Å is ~25% higher than the red, with a 150 Å width for the convolving Gaussian function.

[18] https://c3.lbl.gov/es/#id22

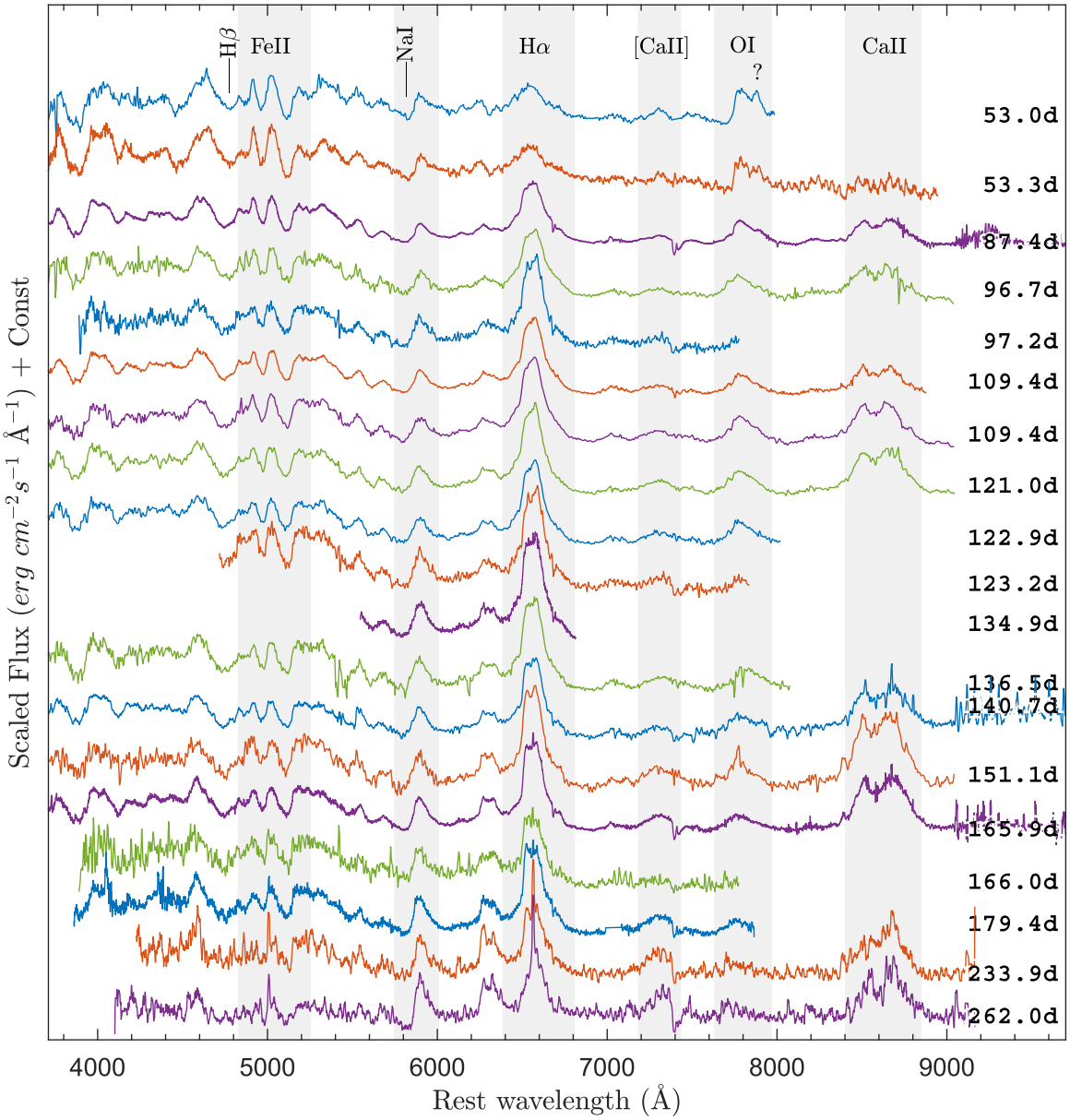


Figure 12. Rest-frame spectral evolution of ASASSN-15nx, ordered by age with respect to the explosion epoch JD 2457219.10. Prominent lines of hydrogen (Hα, Hβ), iron (Fe II $\lambda\lambda$ 4924, 5018, 5169), sodium (Na I λ5890), calcium, and oxygen are marked. Spectra with low SNR have been binned in wavelength to reduce the noise.

The set of atomic species used to generate the synthetic spectrum are H I, He I, O I, Fe II, Ti II, Sc II, Ca II, Ba II, Na I, and Si II. As noted above, ASASSN-15nx exhibits an unusual, triangular Hα emission with a weak absorption feature on the blue side that is not consistent with a P-Cygni profile. The Hβ profile is also unusually broad and extended, which SYNOW could not reproduce with a single Hβ component using any combination of expansion velocity and optical depth profile. Therefore, the Hα and Hβ line region have been masked in the synthetic spectrum. Apart from the nebular-like emission features of Ca II and O I, for which SYNOW is not applicable, many of the spectral features are reasonably well-reproduced—except for the Sc II features at 4274 and 4670 Å.

In the SYNOW model, the absorption feature near 6300 Å, which appears to form the absorption component of the P-Cygni profile associated with Hα, is reproduced by Si II (6355 Å). The Si II velocity is same as the photospheric velocity ($\sim$3.3 $\times$ 10^3 km s^{-1}) found for the other metal lines, affirming the line identification and suggesting that there is little or no absorption component associated with Hα.

5.2. Comparison of Spectra

We compare spectra of ASASSN-15nx to other Type II SNe at three different phases (53.0 days, 121.0 days, 262.0 days), as shown in Figures 14–16. Figure 14 shows the comparisons of the 53.0 day spectrum. Apart from the Hα profile, the spectral features broadly resemble most of the other SNe II spectra in the comparison sample. The Hα profile of ASASSN-15nx is significantly weaker and unusually triangular in shape, compared to other SNe II. For instance, normal SNe II at $t \approx 53$ days have a mean Hα equivalent width of $\sim$157 Å (Gutiérrez et al. 2017), whereas we find a significantly lower value of $\sim$117 Å for ASASSN-15nx and it stays systematically weak throughout the evolution. P-Cygni Hα profiles with an absorption component are

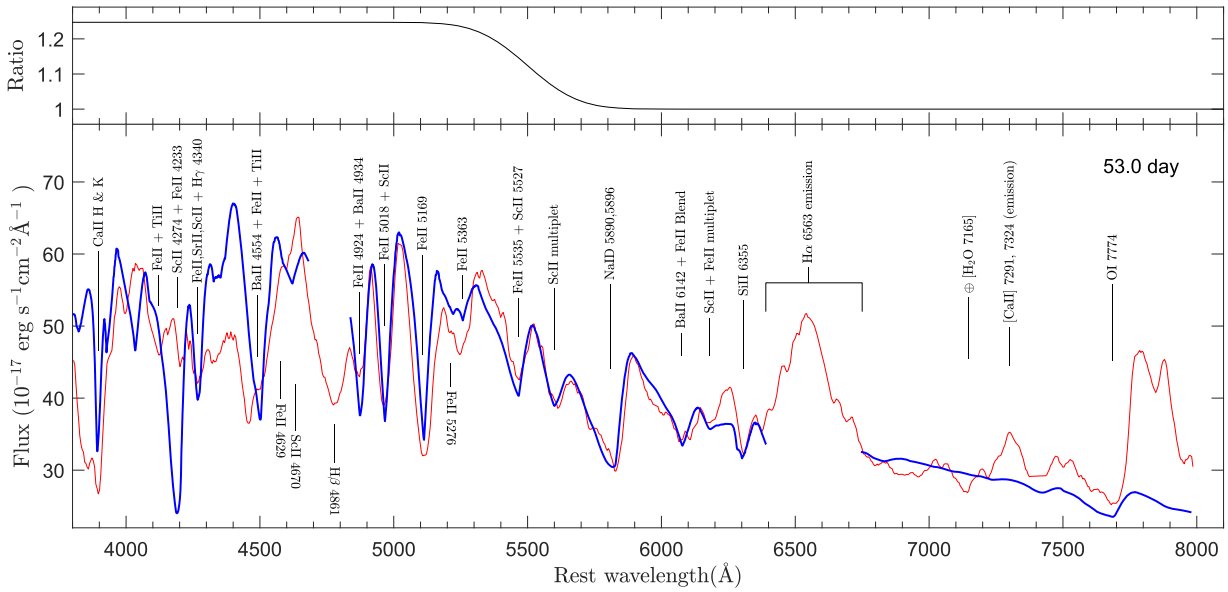


Figure 13. SYNOW model (blue) of the $t = 53.0$ day spectrum of ASASSN-15nx (red). Observed fluxes are corrected for extinction. All ASASSN-15nx spectra show a break in the continuum near 5500 Å, where the blue side has a higher flux level. To reproduce this feature, the model continuum is multiplied by the Gaussian convolved step function shown in the top panel.

common for most SNe II at this phase. However, the absorption component of the Hα profile appears to be non-existent for ASASSN-15nx, as in the SYNOW model discussed above, where the absorption feature blueward of the Hα emission is identified as Si II. The weakening of the Hα absorption component has generally been seen for luminous and fast-declining SNe IIL (see, e.g., Gutiérrez et al. 2014), such as SN2014G, SN1998S, and SN1979C (shown in Figure 14), and the absence of this absorption component in ASASSN-15nx is consistent with this trend. The Hα profile for ASASSN-15nx also has an unusually triangular peak, compared to other known SNe II, including SNe II-L. The doubly peaked and exceptionally strong O I feature near 7700 Å is also not seen in any of the comparison spectra. The spectrum of PTF10iam, whose early-phase light curve closely resembles ASASSN-15nx (see Figure 6), is also shown in Figure 14. Apart from a weak and irregularly shaped Hα profile, the spectrum of PTF10iam does not show any other similarities with ASASSN-15nx.

In Figure 15, we compare the 121.0 day spectrum with three other SNe II spectra at a similar age. The comparison spectra are specifically selected to show some form of irregularities or unusual shapes in their Hα profiles. The ASASSN-15nx spectrum still has weaker Hα emission. In the inset of the Figure 15, we zoom in on the Hα line, scaling each spectra to the line peak. Unlike other SNe, the continuum of ASASSN-15nx on the blue side of Hα has a higher flux level than on the red side. SNe 1999em and 2013ej both show asymmetric, possibly double-peaked components for Hα. Such profiles are often attributed to a bipolar distribution of ^{56}Ni in a spherically symmetric hydrogen envelope (Elmhamdi et al. 2003; Bose et al. 2015a). Similar asymmetric Hα emission due to aspherical ^{56}Ni distribution has also been observed in SNe 1987A (Utrobin et al. 1995) and 2004dj (Chugai 2006). The Hα line profile of ASASSN-15nx appears to be even more complicated and may also be composed of more than one component—though if so, they are not clearly separable. The wedge-shaped peak of ASASSN-15nx is similar to that of the Type II-L/n SN 1998S (Leonard et al. 2000), although the latter has a broader emission profile.

In Figure 16, we compare the 262 day spectrum with three other nebular-phase spectra of Type II SNe. ASASSN-15nx continues to have a weak and triangular Hα profile. The nebular phase features, like forbidden [O I] near 6330 Å and [Ca II] near 7300 Å, are significantly weaker than in the other SNe. The Na I D feature near 5900 Å and the marginally visible Fe II feature near 5000 Å are comparable in strength to those of other SNe II.

5.3. Evolution of Spectral Features

In Figure 17, we show the spectral regions centered on Hα and Hβ in velocity domain. The Fe II multiplets ($\lambda\lambda$ 4924, 5018, 5169) do not show any significant evolution until the 233.9 day spectrum. The Si II (6355 Å) absorption feature identified by SYNOW in the 53 day spectra is not detectable from 87 days and onward. In the same wavelength range, the [O I] emission lines ($\lambda\lambda$ 6300, 6364; indicated in the figure) start to appear and become stronger at later times. For a typical Type II SN, the forbidden [O I] emission is seen only in nebular phase spectra at $t \sim 150$ day. The Hα profiles show a break or an abrupt change in slope on the blue wing of the line profile in all the spectra following day 87. This feature is marked as "A_1" in Figure 17 and in the inset of Figure 15. The position of the A_1 feature is blueshifted by $\sim 3.60 \pm 0.25 \times 10^3$ km s^{-1} from the Hα rest frame and remains almost unchanged after it appears at day 87. We also find a similar kink marked as "A_2" in the blue wing of the Hβ profile. Interestingly, this feature also appeared from day 87 onwards and is also blueshifted by $\sim 3.60 \times 10^3$ km s^{-1} with respect to Hβ. The simultaneous appearance of A_1 and A_2 at consistent velocities implies that the features must have common association with H I, rather than any possible blending with other spectral lines. However, the structural configuration of the H I materials needed to produce such an unusual feature is unclear.

The Hα profile shows an atypical triangular emission in the 53 day spectra, and then develops a peculiar wedge-shaped top at ~87–123 days. After this phase, the emission-top shows irregular, possibly multi-component emission features. The

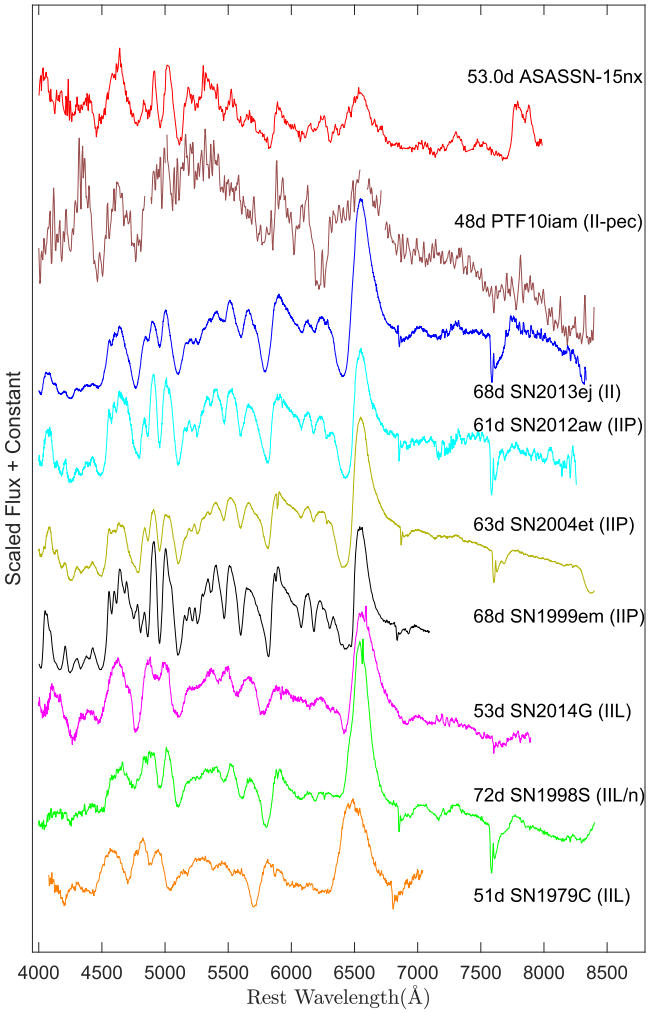


Figure 14. Comparison of the 53.0 day spectrum of ASASSN-15nx to other Type II SNe 2013ej (Bose et al. 2015a), 2012aw (Bose et al. 2013), 2004et (Sahu et al. 2006), 1999em (Hamuy et al. 2001), 2014G Terreran et al. (2016), 1998S (Leonard et al. 2000; Fassia et al. 2001), PTF10iam (Arcavi et al. 2016), and 1979C (Branch et al. 1981) at similar ages. All comparison spectra are corrected for extinction and redshift. For PTF10iam, the regions contaminated by host emission lines are masked.

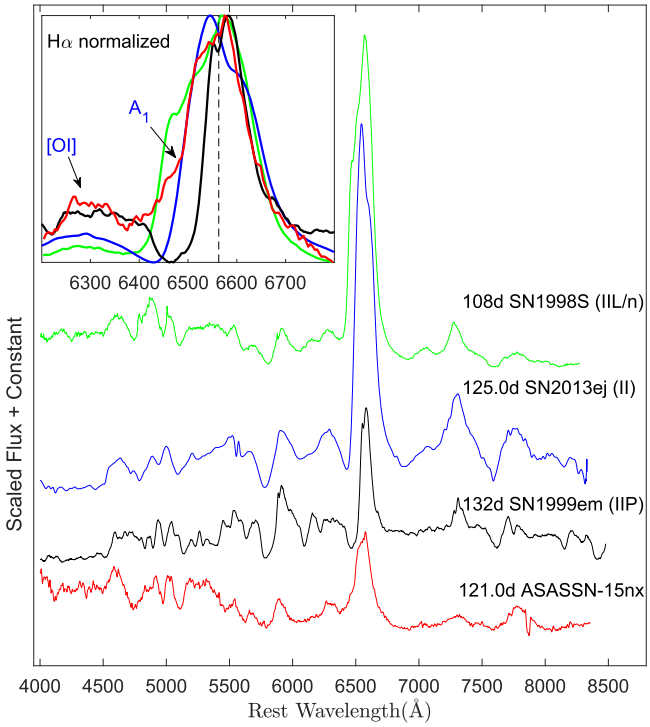


Figure 15. Same as Figure 14, but for the 121.0 day ASASSN-15nx spectrum. The inset shows the Hα region only, scaled to the peaks of the Hα profiles.

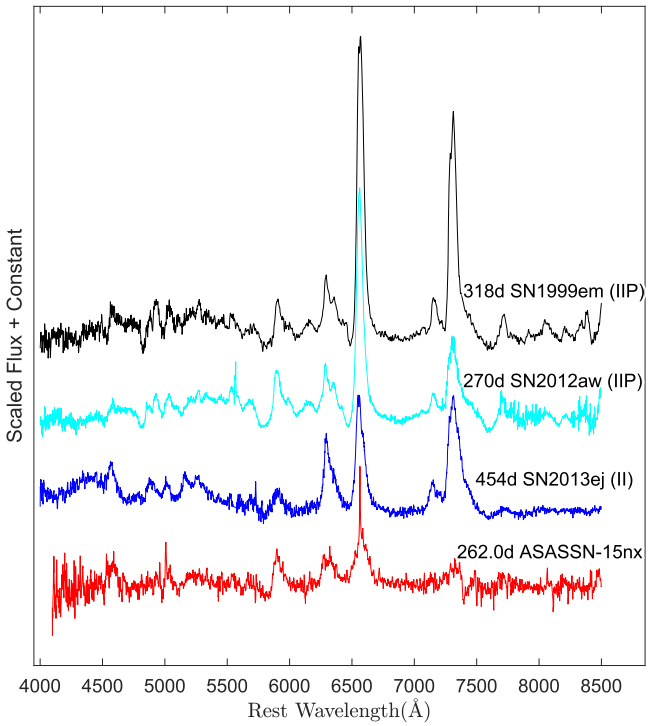


Figure 16. Same as Figure 14, but for a late-phase (262.0 day) spectrum of ASASSN-15nx.

apparent absorption feature near 6400 Å, which can be seen throughout the evolution may be due to the Si II absorption in the 53 day spectra and the [O I] emission feature after 87 days. This would imply that the Hα line lacks the P-Cygni absorption component expected from a typical SN atmosphere. The Hβ absorption is unusually broad and extended as compared to other SNe II (see Figures 14 and 15), which the SYNOW model cannot fit with a single H I component. It is possible that multiple Hβ absorption components are blended together to produce the broad feature. Such a scenario, with two H I components resulting in broader Hα and Hβ absorption profiles, has been seen in SNe 2012aw (Bose et al. 2013) and 2013ej (Bose et al. 2015a). However, this explanation may not hold for ASASSN-15nx, due to the missing Hα absorption feature.

Figures 18 and 19 illustrate the spectroscopic velocity evolution of ASASSN-15nx. In Figure 18, we show the Hβ and Fe II velocities, using the blueshifted absorption feature for each line. This includes no corrections for possible blended components. The Hβ velocity evolution is puzzling, rising from 5.0×10^3 km s^{-1} at day 53 to $\sim6.6\times10^3$ km s^{-1} at day 87, and then continuing to increase. The peculiar Hβ velocity evolution may indicate the presence of high-velocity components within the absorption profiles. An interaction of outer ejecta with CSM can produce such high-velocity components, which are expected to remain almost constant in velocity throughout the evolution (Chugai et al. 2007; Bose et al. 2015a; Gutiérrez et al. 2017). If the high-velocity component were strong enough, and the regular Hβ component continued to weaken, then the effective minima of

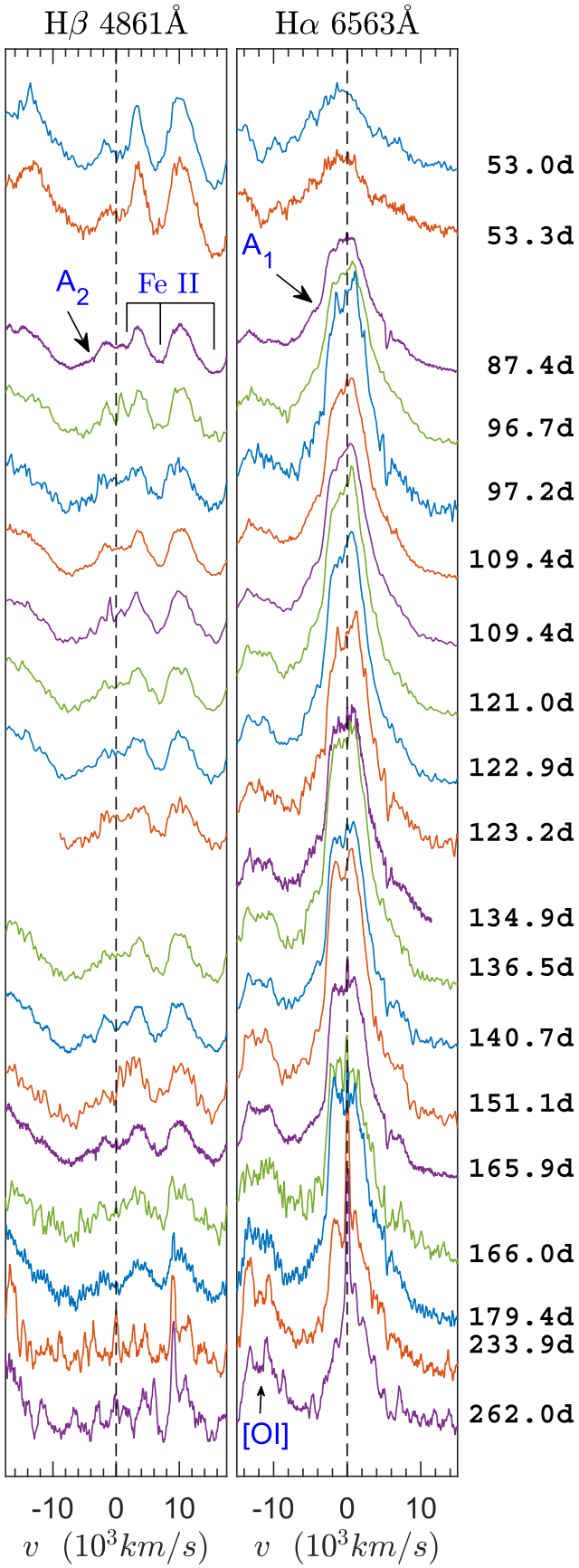


Figure 17. Spectroscopic evolution in the velocity domain corresponding to the Hα and Hβ rest wavelengths. The Fe II multiplets are also in the Hβ window.

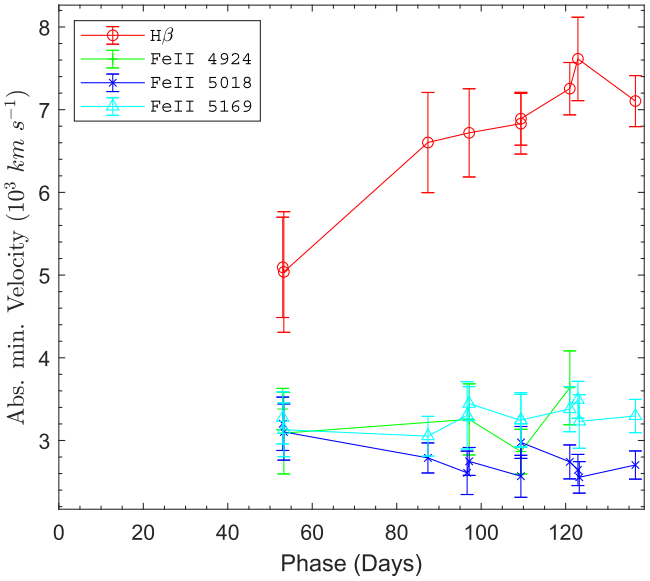


Figure 18. Velocity evolution of the Hβ, and Fe II lines for ASASSN-15nx. The velocities are estimated from the blueshift of the apparent absorption minima. No attempt has been made to decouple any possible contamination from other lines or high-velocity features.

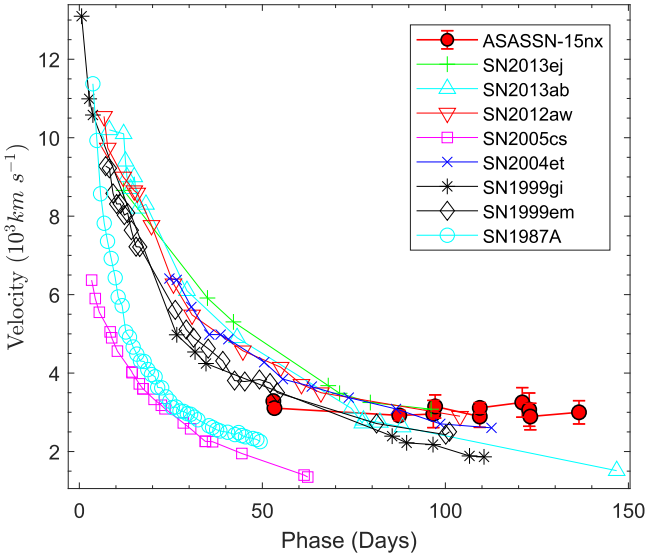


Figure 19. Photospheric velocity evolution (v_{ph}) of ASASSN-15nx, as compared with other well-studied Type II SNe. The v_{ph} is estimated by the Fe II absorption trough velocities.

the blended trough could show an increasing blueward shift, as we see in ASASSN-15nx. On the other hand, the Fe II lines, which are generally regarded as good tracers of the photosphere, show almost no variation during the entire spectral evolution. In Figure 19, the Fe II line velocities of ASASSN-15nx are compared to other Type II SNe. Unlike the other SNe, the Fe II velocity of ASASSN-15nx remains almost unchanged at $\sim 3.1 \times 10^3$ km s^{-1}.

6. Summary of Peculiarities

ASASSN-15nx exhibits a number of unusual features, which can be summarized as follows.

1. The peak magnitude of ~ -20 lies in the luminosity "gap" between normal CCSNe and SLSNe.
2. It has a uniquely long-lived, post-peak linear light curve decline with a steep slope of 2.5 mag (100 day)$^{-1}$ (i.e., an exponential decline in flux $\propto e^{-t/43\ \mathrm{day}}$) until the end. The perfectly linear light curve extended to the end of observations at day 262. This is much longer than any known SNe IIP/L, which always show a change in light curve slope at around 100 days after maximum light, marking the transition to a ^{56}Co radioactive decay tail with a slope of 0.98 mag (100 day)$^{-1}$.
3. The broadband colors are almost constant and remain blue after 50 days. Equivalently, the blackbody temperature monotonically decreases until day 50, as expected, reaching at $T \sim 5.8$ kK. However, after this epoch, we see an upward trend in the temperature, which reaches a value of $\sim$7.5 kK near day 135, before it again starts to decrease. Such an evolution has not been observed in any other SNe II.
4. The spectra of ASASSN-15nx shows unique, triangular Hα emission profile throughout its evolution. The strength of the Hα emission is weak, compared to a typical SN II-P/L.
5. The Hα profile shows no evidence for an associated P-Cygni absorption trough. The apparent absorption minima on the blue wing appears to be due to the presence of a Si II feature at day 53, and then an [O I] feature at later times.
6. Nebular spectral features like O I (7774 Å), [Ca II] ($\lambda\lambda$ 7291, 7324) and [O I] ($\lambda\lambda$ 6300, 6364) appeared earlier than in a typical SN II-P/L. For example, the [O I] features in typical SNe IIP appear after $\sim$150 days, while they are detectable starting at day 87 in ASASSN-15nx. Due to the presence of these features, the spectra of ASASSN-15nx appear more evolved than a typical SN II at a similar age.
7. The O I (7774 Å) feature show a double-peaked emission at day 53. The unidentified redder component is much weaker at 87.4 days and completely disappears in later epochs.
8. The spectra all show an abrupt continuum break near 5500 Å. The blue continuum is systematically brighter than the red (e.g., by $\sim$24% at 53.0 days).
9. There is a break in the blue wing of the both Hα and Hβ profiles (marked as "A_1" and "A_2" in Figures 17 and 15), starting at day 87, with a blueshifted velocity of $\sim$3.6 $\times 10^3$ km s^{-1}, indicating that both of these features have a common H I origin.
10. The Hβ velocity shows an unusual increasing trend with time. The Hβ absorption profile is also unusually broad and extended. This could not be reproduced by a single H I component in our SYNOW models.
11. The Fe II line velocities show no evolution, while in typical SNe, all line velocities are expected to decay with time.

7. Discussion

We are not aware of a theoretical model that can explain all the peculiarities of ASASSN-15nx. Important questions remain, such as what powers this luminous SN II and how the long-lasting, "perfectly" linear light curve is produced, which are discussed in Sections 7.1 and 7.2. In Section 7.3, we comment on the rate of SNe that are like ASASSN-15nx.

7.1. High ^{56}Ni Mass

One possible scenario for powering ASASSN-15nx is the synthesis of a large amount of radioactive ^{56}Ni. As discussed in Section 4.2, matching the high luminosity requires an exceptionally large amount of ^{56}Ni, $M_{\mathrm{Ni}} = 1.6 \pm 0.2\ M_\odot$. This is significantly higher than normal Type II SNe, which have average M_{Ni} of 0.05 $M_\odot$ and extend to, at most, $\sim$0.1–0.2 $M_\odot$ (see, e.g., Müller et al. 2017). For stripped-envelope SNe, it can be as high as 0.6–0.7 $M_\odot$ (e.g., for Type Ic SN 2011bm; Valenti et al. 2012). The best-fit model also requires inefficient γ-ray trapping, with $t_{0\gamma} \approx 71$ days. For comparison, normal SNe IIP are consistent with complete trapping (i.e., $t_{0\gamma} \to \infty$), and for SNe Ia, $t_{0\gamma} \approx 40$ days (Wygoda et al. 2017). The value of $t_{0\gamma}$ for ASASSN-15nx implies that the envelope is inefficient at thermalizing the γ-rays. This is also consistent with weak Hα emission, because the hydrogen content in an SN ejecta is the dominant source of the γ-ray opacity.

The implied high ^{56}Ni mass and the short gamma-ray escape time of $t_0 \sim 70$ days constrain the ejecta structure. The γ-rays must escape the region in the ejecta where the ^{56}Ni is concentrated, allowing a constraint on the iron velocities. The gamma-ray escape time of a homogeneous ball of iron with outer velocity v_{edge} and mass M is

$$t_0 = 85\ \mathrm{day} \left(\frac{M}{1.5\ M_\odot}\right)^{0.5} \left(\frac{v_{\mathrm{edge}}}{5 \times 10^3\ \mathrm{km\ s^{-1}}}\right)^{-1}, \quad (1)$$

using an effective γ-ray opacity of $\kappa_\gamma = 0.025$ cm^2 g^{-1} (Swartz et al. 1995; Jeffery 1999). This implies that the produced iron has to be distributed to velocities extending beyond $\sim 5 \times 10^3$ km s^{-1}. Moreover, there is no room for significant additional mass at velocities $\lesssim 5 \times 10^3$ km s^{-1}. Assuming that the hydrogen carries most of the energy, it is useful to write the constraint for additional mass at higher velocities in terms of the total energy. The gamma-ray escape time from the center of a homogeneous ball of hydrogen with kinetic energy E and mass M is

$$t_0 = 87\ \mathrm{day} \left(\frac{M}{2\ M_\odot}\right) \left(\frac{E}{10^{51}\ \mathrm{erg}}\right)^{-1/2}. \quad (2)$$

For example, a Ni mass of $1.5 M_\odot$ extending to velocity 7×10^3 km s^{-1}, embedded in a hydrogen ball of $1 M_\odot$ extending to 16×10^3 km s^{-1}, would have a total gamma-ray escape time of 70 days and total energy of 2×10^{51} erg, which are not inconceivable.

To gain more insight into the envelope properties, we attempted a simple semi-analytical model described by Arnett (1980) and Arnett & Fu (1989). The formulation and implementation of this model are discussed in Bose et al. (2015a) and references therein. This is a single-component envelope model with radioactive ^{56}Ni confined at the center. This model is not fully applicable for ASASSN-15nx, as we observe no clear photospheric phase. However, by simply applying the model, we obtain an estimated envelope mass of $\sim$0.8–2.0 $M_\odot$ with a thermal energy of $\approx 1.5 \times 10^{51}$ erg. It must be emphasized that these parameters are the upper limits; as these values increase, the model light curves show more sustained and prominent photospheric phases. For these parameters, the ejecta becomes optically transparent at $\sim$45 days, which coincides with the break seen in the B-band light curve, after which the light curve is solely powered by the ^{56}Ni $\to$

^{56}Co → ^{56}Fe decay chain. This low ejecta mass is consistent with the inefficient γ-ray trapping required for the radioactive decay model. Although we see the presence of H, O and Ca lines in the late spectra, as we see in typical SNe II with large ejecta masses, these lines are much weaker than typical SNe II (see Figure 16), also suggestive of a low ejecta mass.

The large ^{56}Ni mass is consistent with the correlation between $M_{\rm Ni}$ and V-band luminosity, as shown in Figure 11. In this scenario, ASASSN-15nx might have produced a tremendous amount of radioactive ^{56}Ni with a significantly stripped envelope. However, it is not clear which mechanism could produce such a large mass of ^{56}Ni. One possible scenario is a thermonuclear explosion in a CCSNe (Kushnir 2015b; Kushnir & Katz 2015), which would produce a wide distribution of ^{56}Ni masses (Kushnir 2015a). Pair instability explosions can also produce a large amount of ^{56}Ni with a wide range of luminosities, but they are also predicted to produce extended light curves (Kasen et al. 2011) different from that observed for ASASSN-15nx.

The possible production of a large amount of ^{56}Ni ($\sim$0.6 $M_{\odot}$) in luminous and fast-declining SN II-L SN 1979C was raised by Doggett & Branch (1985), Wheeler et al. (1987), and Young & Branch (1989). Later, Blinnikov & Bartunov (1993) showed that the high luminosity of SN 1979C in its photospheric phase could also be explained by the reprocessing of UV light into optical by an extended low-mass hydrogen–helium envelope. However, despite the similarities in luminosity between ASASSN-15nx and SN 1979C in its early phases, there is a clear break in the light-curve slope of SN 1979C near 70 days that indicates a change in the dominant energy source. As the ejecta becomes optically thin, the UV reprocessing ceases. However, ASASSN-15nx does not show such a break, making it challenging to explain the prolonged, "perfectly" linear light curve of ASASSN-15nx solely by reprocessing of UV energy.

Another factor that may affect the ^{56}Ni mass estimate is the asymmetry of the ejecta. Höflich et al. (1999) showed that, for Type Ic-BL supernova 1998bw, an ejecta axis ratio of 2 may produce 2 mag of variation in peak luminosity between the polar and equatorial directions. Polarimetric observations of SN 1998bw were also consistent with asymmetry in the ejecta of 1998bw. Polarimetry studies suggest that CCSNe, particularly those with relatively small envelope masses, may exhibit significant asymmetry in their ejecta (see, e.g., Wang et al. 2001). If the ejecta of ASASSN-15nx were highly asymmetrical and viewed at a favorable angle, the actual amount of synthesized ^{56}Ni might be substantially reduced from the current estimate and produce its high peak luminosity. On the other hand, there is no strong evidence of asymmetry in the [O I] ($\lambda\lambda$ 6300, 6364) nebular lines, as suggested by Taubenberger et al. (2009, 2013). However, quantitative modeling is needed to investigate whether an asymmetric model could explain the prolonged linear light-curve and spectroscopic features of ASASSN-15nx.

Synthesizing a large amount of radioactive ^{56}Ni normally should also lead to nebular-phase spectra rich with iron-group elements, as seen in Type Ia SNe, but this doesn't appear to be the case with ASASSN-15nx. This could pose a serious challenge to the high ^{56}Ni mass scenario, and nebular-phase spectral modeling would be needed to examine it further.

7.2. CSM Interaction

An alternative to the radioactive decay model is strong CSM interactions. In these models, the structure and distribution of the CSM can determine the shape of the light curves. As in SNe IIn (Schlegel 1990), which are characterized by narrow emission lines (FWHM $\sim$ few hundreds of km s^{-1}) in the spectra, strong interactions are thought to be responsible for powering their prolonged and often luminous light curves (e.g., Smith et al. 2008a; Rest et al. 2011). Sometimes ejecta–CSM interactions can lead to steeply declining light curves, as has been proposed for SN 2009jp (jet–CSM interaction; Smith et al. 2012a) and ASASSN-15no (Benetti et al. 2018). PTF10iam (Arcavi et al. 2016), which has early light curve features similar to ASASSN-15nx, may also be explained by interaction.

The density profile of the CSM can be sculpted to produce the observed light curve of ASASSN-15nx. In ASASSN-15nx, we do not see narrow- or intermediate-width emission lines from the expanding shock driving photo-ionization of the remaining CSM. It is possible to miss such emission lines if those were only present before our spectroscopic observations began at 53.0 days. However, this seems unlikely, as the continuous and linear decline of the light curve indicates a single dominant powering source throughout the evolution, which should produce similar narrow emission lines at later phases if they were present earlier. On the other hand, sometimes CSM signatures may also remain hidden if there is asymmetry or the CSM has a velocity of several thousands of km s^{-1}.

Some of the spectral features in ASASSN-15nx can be attributed to indirect signatures of CSM interaction. The SYNOW model could not reproduce the broad and extended Hβ absorption feature with a single, regular H I component, and the steadily increasing Hβ absorption velocity may indicate the presence of a blended high-velocity absorption component. In the case of CSM interactions relatively weaker than SNe IIn, the enhanced excitation of outer ejecta can produce high-velocity H I absorption features (e.g., SNe 1999em, 2004dj (Chugai et al. 2007), 2009bw (Inserra et al. 2012)) without producing narrow emission lines. In some other cases, the interaction signature can remain blended with regular H I P-Cygni profiles: e.g., SNe 2012aw (Bose et al. 2013) and 2013ej (Bose et al. 2015a), where the two components can not be resolved individually, but result in broadening of Hα and Hβ absorption profiles. In ASASSN-15nx, as the strength of the regular component decays, the effective position of the blended absorption trough would shift blueward. However, this would also require a similar high-velocity absorption feature in the Hα profile, which does not seem to be present—instead, the entire absorption feature is missing in the SN. Another possibility is that this peculiar Hα emission line profile might be composed of multiple components arising from CSM interactions.

The unusual rise in temperature from 50 to 135 days, which also coincides with the period of steady increase in the Hβ velocity, might also be suggestive of CSM interaction. The increase in temperature could be due to the additional energy input from the ejecta interacting with CSM. The unusual break in the spectral continuum near 5500 Å may be also explained via CSM interaction. Similar enhancements of the blue continuum have been seen in some strongly interacting SNe, such as SNe 2011hw (Smith et al. 2012b), 2006jc (Smith et al. 2008b), and 2005ip (Smith et al. 2009). The blue excess could be due to the blending of large number of broad and intermediate-width lines produced by the CSM interaction (Chugai 2009; Smith et al. 2012b). In the case of SN 2005ip, the CSM lines were narrow enough to be seen forming the blue excess.

Another possible signature indicative of CSM interaction is the A_1 and A_2 pair of features, discussed in Section 5.3 (see Figures 17, 15). The favorable aspect of this pair of features is that

both are located at the same blueshifted velocity of $\sim 3.6 \times 10^3$ km s^{-1}, implying a common origin. This may indicate that these H I features are produced by ejecta interacting with a clump or a shell of material. However, it may be difficult to explain an interaction-powered light curve showing only these weak spectral signatures.

7.3. Rate for SNe Similar to ASASSN-15nx

We can make two simple estimates of the rate of transients that are similar to ASASSN-15nx: one based on a crude model of the ASAS-SN survey, and the other using a simple scaling based on the number of Type Ia SNe in ASAS-SN. Roughly speaking, ASAS-SN detects $V < 17$ mag transients, which means that ASASSN-15nx could be detected to a comoving distance of ~ 214 Mpc, corresponding to a volume of $V = 0.041$ Gpc^3. The rate implied by finding one such event is

$$r = 25\left(\frac{4\pi}{\Omega}\right)\left(\frac{\text{years}}{t_{\text{eff}}}\right), \quad (3)$$

where $\Omega \simeq 2\pi$ is the fraction of the sky being surveyed for SNe at any given time and t_{eff} is the effective survey time. Roughly speaking, ASAS-SN has been running for 2.7 years, but finds only 70% of the $V < 17$ mag SNe visible in its survey area, so $t_{\text{eff}} \simeq 1.8$ years. Combining these factors gives a rough rate estimate of $r \simeq 28$ Gpc^{-3} yr^{-1}. Alternatively, ASASSN-15nx is about one magnitude more luminous than a typical Type Ia SNe, implying an effective survey volume to find events like ASASSN-15nx that is four times greater than for Type Ia SNe. In its first 2.7 years, ASAS-SN found a total of 449 Type Ia SNe, so the rate for events like ASASSN-15nx should be $r = r_{\text{Ia}}/4/449$, correcting for the larger volume for detecting ASASSN-15nx (4) and the ratio of the numbers of the two events (1 : 449). The Type Ia SNe rate is $r_{\text{Ia}} \simeq 3 \times 10^4$ Gpc^{-3} yr^{-1} (Li et al. 2011a), so $r \simeq 17$ Gpc^{-3} yr^{-1}, which is in good agreement with the first estimate. Thus, the rate of transients similar to ASASSN-15nx is comparable to that for hydrogen-poor (Type I) SLSNe $r_{\text{SLSN-I}} = 91^{+76}_{-36}$ Gpc^{-3} yr^{-1} derived by Prajs et al. (2017), raising the possibility that the previously identified luminosity "gap" between normal CCSNe and SLSNe might be due to observational selection effects.

We thank A. Gal-Yam and M, Fraser for helpful comments. We are grateful to I. Arcavi for providing us the spectroscopic data for PTF10iam. S.B., S.D., and P.C. acknowledge Project 11573003, supported by the NSFC. S.B. is partially supported by the China Postdoctoral Science Foundation through grant No. 2016M600848. A.P., L.T., S.B., and N.E.R. are partially supported by the PRIN-INAF 2014 project "Transient Universe: Unveiling New Types of Stellar Explosions with PESSTO." C.S.K., K.Z.S., and T.A.T. are supported by the U.S. National Science Foundation (NSF) though grants AST-1515927 and AST-1515876. We acknowledge support by the Ministry of Economy, Development, and Tourism's Millennium Science Initiative through grant IC120009, awarded to The Millennium Institute of Astrophysics, MAS, Chile (J.L.P., C.R.-C.) and from CONICYT through FONDECYT grants 3150238 (C.R.-C.) and 1151445 (J.L.P.). Support for N.S. was provided by the NSF through grants AST-1312221 and AST-1515559 to the University of Arizona. A.M.G. acknowledges financial support by the University of Cádiz though grant PR2017-64.

This work is based on observations made with the Large Binocular Telescope. The LBT is an international collaboration among institutions in the United States, Italy, and Germany. The LBT Corporation partners are: the University of Arizona, on behalf of the Arizona university system; the Istituto Nazionale di Astrofisica, Italy; the LBT Beteiligungsgesellschaft, Germany, representing the Max Planck Society, the Astrophysical Institute Potsdam, and Heidelberg University; the Ohio State University; and the Research Corporation, on behalf of the University of Notre Dame, the University of Minnesota, and the University of Virginia. We thank the staff at the MMT Observatory for their assistance with the observations. Observations using Steward Observatory facilities were obtained as part of the large observing program, AZTEC: Arizona Transient Exploration and Characterization. Some of the observations reported in this paper were obtained at the MMT Observatory, a joint facility of the University of Arizona and the Smithsonian Institution. Partially based on observations collected at Copernico telescope (Asiago, Italy) of the INAF—Osservatorio Astronomico di Padova.

This research was made possible through use of the AAVSO Photometric All-Sky Survey (APASS), funded by the Robert Martin Ayers Sciences Fund. This research uses data obtained through the Telescope Access Program (TAP), which has been funded by "The Strategic Priority Research Program: the Emergence of Cosmological Structures" of the Chinese Academy of Sciences (grant No. 11 XDB09000000) and the Special Fund for Astronomy from the Ministry of Finance.

We thank the Las Cumbres Observatory and its staff for their continuing support of the ASAS-SN project. We are grateful to M. Hardesty of the OSU ASC technology group. ASAS-SN is supported by the Gordon and Betty Moore Foundation through grant GBMF5490 to the Ohio State University and NSF grant AST-1515927. Development of ASAS-SN has been supported by NSF grant AST-0908816, the Mt. Cuba Astronomical Foundation, the Center for Cosmology and AstroParticle Physics at the Ohio State University, the Chinese Academy of Sciences South America Center for Astronomy (CASSACA), the Villum Foundation, and George Skestos. This paper uses data products produced by the OIR Telescope Data Center, supported by the Smithsonian Astrophysical Observatory.

The Liverpool Telescope is operated on the island of La Palma by Liverpool John Moores University in the Spanish Observatorio del Roque de los Muchachos of the Instituto de Astrofisica de Canarias, with financial support from the UK Science and Technology Facilities Council (STFC). This paper used data obtained with the MODS spectrographs built with funding from NSF grant AST-9987045 and the NSF Telescope System Instrumentation Program (TSIP), with additional funds from the Ohio Board of Regents and The Ohio State University Office of Research. The ModsIDL spectral data reduction reduction pipeline was developed in part with funds provided by NSF Grant AST-1108693. Partially based on observations collected at Copernico telescope (Asiago, Italy) of the INAF—Osservatorio Astronomico di Padova. The Joan Oró Telescope (TJO) of the Montsec Astronomical Observatory (OADM) is owned by the Catalan Government and operated by the Institute for Space Studies of Catalonia (IEEC).

Software: MATLAB, Python, IDL, SYNOW (Fisher et al. 1997, 1999; Branch et al. 2002), Astropy (Astropy Collaboration et al. 2013), IRAF (Tody 1993), LT pipeline (Barnsley et al. 2012; Piascik et al. 2014), DAOPHOT (Stetson 1987), FOSCGUI, modsIDL pipeline.

Table 1
Photometry of ASASSN-15nx

UT Date	JD-2457,000	Phase[a] (days)	B (mag)	V (mag)	R (mag)	I (mag)	g (mag)	r (mag)	i (mag)	Telescope[b] /Inst.
2015 Jul 16.42	219.92	0.80	⋯	>16.910	⋯	⋯	⋯	⋯	⋯	ASASSN
2015 Jul 19.42	222.92	3.71	⋯	16.540 ± 0.100	⋯	⋯	⋯	⋯	⋯	ASASSN
2015 Jul 21.41	224.91	5.65	⋯	16.370 ± 0.070	⋯	⋯	⋯	⋯	⋯	ASASSN
2015 Jul 23.40	226.90	7.59	⋯	16.200 ± 0.080	⋯	⋯	⋯	⋯	⋯	ASASSN
2015 Aug 08.63	243.13	23.37	⋯	15.830 ± 0.130	⋯	⋯	⋯	⋯	⋯	ASASSN
2015 Aug 09.62	244.12	24.33	⋯	16.000 ± 0.060	⋯	⋯	⋯	⋯	⋯	ASASSN
2015 Aug 09.73	244.23	24.44	16.183 ± 0.047	15.981 ± 0.016	⋯	15.369 ± 0.022	⋯	⋯	⋯	LCO
2015 Aug 12.47	246.97	27.10	⋯	16.010 ± 0.046	⋯	15.375 ± 0.039	⋯	⋯	⋯	LCO
2015 Aug 13.60	248.10	28.20	⋯	15.940 ± 0.060	⋯	⋯	⋯	⋯	⋯	ASASSN
2015 Aug 15.16	249.66	29.72	16.344 ± 0.042	16.037 ± 0.019	⋯	15.380 ± 0.026	⋯	⋯	⋯	LCO
2015 Aug 17.32	251.82	31.82	⋯	16.120 ± 0.060	⋯	⋯	⋯	⋯	⋯	ASASSN
2015 Aug 18.15	252.65	32.63	16.504 ± 0.059	16.132 ± 0.023	⋯	15.466 ± 0.025	⋯	⋯	⋯	LCO
2015 Aug 21.32	255.82	35.71	⋯	⋯	⋯	15.575 ± 0.036	⋯	⋯	⋯	LCO
2015 Aug 23.31	257.81	37.65	⋯	16.340 ± 0.080	⋯	⋯	⋯	⋯	⋯	ASASSN
2015 Aug 24.32	258.82	38.63	16.888 ± 0.058	16.357 ± 0.027	⋯	15.611 ± 0.025	⋯	⋯	⋯	LCO
2015 Aug 27.38	261.88	41.60	17.025 ± 0.070	16.443 ± 0.015	⋯	15.665 ± 0.028	⋯	⋯	⋯	LCO
2015 Aug 30.29	264.79	44.43	⋯	⋯	⋯	15.680 ± 0.033	⋯	⋯	⋯	LCO
2015 Sep 02.28	267.78	47.34	17.402 ± 0.078	16.637 ± 0.021	⋯	15.817 ± 0.036	⋯	⋯	⋯	LCO
2015 Sep 04.66	270.16	49.66	17.405 ± 0.080	16.625 ± 0.031	⋯	15.889 ± 0.027	⋯	⋯	⋯	LCO
2015 Sep 11.33	276.83	56.15	17.580 ± 0.157	16.923 ± 0.018	⋯	⋯	⋯	⋯	⋯	LCO
2015 Sep 17.33	282.83	61.98	17.579 ± 0.055	17.055 ± 0.022	⋯	16.212 ± 0.020	⋯	⋯	⋯	LCO
2015 Sep 22.61	288.11	67.12	⋯	⋯	⋯	16.247 ± 0.132	⋯	⋯	⋯	LCO
2015 Sep 26.23	291.73	70.63	17.974 ± 0.106	17.233 ± 0.031	⋯	16.540 ± 0.041	⋯	⋯	⋯	LCO
2015 Sep 28.60	294.10	72.94	17.870 ± 0.129	17.302 ± 0.056	⋯	16.560 ± 0.041	⋯	⋯	⋯	LCO
2015 Oct 02.42	297.92	76.66	⋯	17.401 ± 0.020	17.250 ± 0.014	16.736 ± 0.014	⋯	⋯	⋯	LOTIS
2015 Oct 03.42	298.92	77.63	⋯	17.496 ± 0.018	17.350 ± 0.009	16.674 ± 0.014	⋯	⋯	⋯	LOTIS
2015 Oct 11.59	307.09	85.57	18.125 ± 0.083	17.559 ± 0.036	⋯	16.851 ± 0.044	⋯	⋯	⋯	LCO
2015 Oct 12.13	307.63	86.10	⋯	⋯	⋯	⋯	17.829 ± 0.005	17.551 ± 0.008	17.464 ± 0.008	NOT
2015 Oct 15.71	311.21	89.58	18.201 ± 0.071	17.757 ± 0.035	⋯	17.002 ± 0.042	⋯	⋯	⋯	LCO
2015 Oct 21.05	316.55	94.78	18.261 ± 0.080	17.872 ± 0.034	⋯	17.072 ± 0.058	⋯	⋯	⋯	LCO
2015 Oct 23.07	318.57	96.74	18.348 ± 0.015	17.823 ± 0.015	17.674 ± 0.022	17.140 ± 0.026	17.948 ± 0.015	17.644 ± 0.021	17.743 ± 0.029	Coper,TJO
2015 Oct 25.88	321.38	99.47	⋯	⋯	⋯	⋯	⋯	⋯	⋯	LCO
2015 Oct 29.40	324.90	102.89	⋯	18.017 ± 0.070	⋯	⋯	⋯	17.927 ± 0.070	17.961 ± 0.076	LCO
2015 Nov 01.10	327.60	105.52	18.459 ± 0.052	17.880 ± 0.035	17.831 ± 0.037	17.371 ± 0.056	⋯	⋯	⋯	TJO
2015 Nov 02.86	329.36	107.23	18.478 ± 0.071	18.045 ± 0.033	⋯	⋯	⋯	17.909 ± 0.027	18.003 ± 0.046	LCO
2015 Nov 05.17	331.67	109.48	18.635 ± 0.024	18.216 ± 0.016	⋯	⋯	18.326 ± 0.014	17.997 ± 0.013	18.130 ± 0.023	Coper
2015 Nov 07.08	333.58	111.34	18.690 ± 0.023	18.092 ± 0.032	17.980 ± 0.029	17.496 ± 0.038	⋯	⋯	⋯	TJO
2015 Nov 07.32	333.82	111.57	⋯	18.303 ± 0.036	18.085 ± 0.021	17.741 ± 0.047	⋯	⋯	⋯	LOTIS
2015 Nov 07.35	333.85	111.60	18.684 ± 0.077	18.262 ± 0.035	⋯	⋯	⋯	18.038 ± 0.026	18.110 ± 0.048	LCO
2015 Nov 08.07	334.57	112.30	18.725 ± 0.020	18.076 ± 0.023	17.897 ± 0.054	17.506 ± 0.035	⋯	⋯	⋯	TJO
2015 Nov 08.32	334.82	112.54	⋯	18.384 ± 0.036	18.144 ± 0.030	17.593 ± 0.028	⋯	⋯	⋯	LOTIS
2015 Nov 09.05	335.55	113.25	18.742 ± 0.023	18.139 ± 0.024	18.023 ± 0.033	17.537 ± 0.029	⋯	⋯	⋯	TJO
2015 Nov 09.32	335.82	113.52	⋯	18.329 ± 0.031	18.165 ± 0.021	17.724 ± 0.031	⋯	⋯	⋯	LOTIS
2015 Nov 10.07	336.57	114.25	18.730 ± 0.042	18.144 ± 0.050	18.013 ± 0.035	17.508 ± 0.040	⋯	⋯	⋯	TJO
2015 Nov 11.32	337.82	115.46	⋯	18.353 ± 0.052	18.164 ± 0.025	17.630 ± 0.035	⋯	⋯	⋯	LOTIS
2015 Nov 12.07	338.57	116.19	18.806 ± 0.022	18.203 ± 0.025	18.087 ± 0.027	17.683 ± 0.036	⋯	⋯	⋯	TJO
2015 Nov 13.05	339.55	117.15	18.839 ± 0.023	18.253 ± 0.024	18.134 ± 0.024	17.622 ± 0.039	⋯	⋯	⋯	TJO

Table 1
(Continued)

UT Date	JD-2457,000	Phase[a] (days)	B (mag)	V (mag)	R (mag)	I (mag)	g (mag)	r (mag)	i (mag)	Telescope[b] /Inst.
2015 Nov 13.30	339.80	117.39	18.754 ± 0.184	18.334 ± 0.033	⋯	⋯	⋯	⋯	18.373 ± 0.047	LCO
2015 Nov 14.32	340.82	118.38	⋯	18.420 ± 0.031	18.209 ± 0.026	17.758 ± 0.032	⋯	⋯	⋯	LOTIS
2015 Nov 17.04	343.54	121.02	⋯	⋯	⋯	⋯	18.568 ± 0.039	18.218 ± 0.018	18.422 ± 0.027	Coper
2015 Nov 17.32	343.82	121.30	⋯	18.440 ± 0.053	18.256 ± 0.031	17.684 ± 0.060	⋯	⋯	⋯	LOTIS
2015 Nov 19.01	345.51	122.94	18.876 ± 0.023	18.491 ± 0.019	⋯	⋯	18.574 ± 0.016	18.251 ± 0.017	18.457 ± 0.019	Coper
2015 Nov 20.32	346.82	124.21	⋯	18.588 ± 0.022	18.361 ± 0.016	17.929 ± 0.024	⋯	⋯	⋯	LOTIS
2015 Nov 22.17	348.67	126.01	18.949 ± 0.107	18.599 ± 0.038	⋯	⋯	⋯	18.411 ± 0.028	18.560 ± 0.053	LCO
2015 Nov 23.32	349.82	127.13	⋯	⋯	⋯	17.936 ± 0.573	⋯	⋯	⋯	LOTIS
2015 Nov 27.32	353.82	131.02	⋯	18.687 ± 0.097	18.815 ± 0.060	18.033 ± 0.047	⋯	⋯	⋯	LOTIS
2015 Nov 28.02	354.52	131.70	⋯	⋯	⋯	⋯	⋯	⋯	⋯	LCO
2015 Nov 29.32	355.82	132.97	⋯	18.825 ± 0.047	18.681 ± 0.040	18.049 ± 0.044	⋯	⋯	⋯	LOTIS
2015 Nov 29.52	356.02	133.16	19.230 ± 0.093	18.739 ± 0.037	⋯	⋯	⋯	18.538 ± 0.039	18.883 ± 0.086	LCO
2015 Nov 30.51	357.01	134.13	19.128 ± 0.074	18.771 ± 0.034	⋯	⋯	⋯	18.570 ± 0.035	18.843 ± 0.057	LCO
2015 Dec 03.02	359.52	136.56	19.207 ± 0.042	18.833 ± 0.026	⋯	⋯	19.082 ± 0.034	18.620 ± 0.016	18.882 ± 0.024	Coper
2015 Dec 03.33	359.83	136.87	⋯	18.951 ± 0.045	18.695 ± 0.031	18.270 ± 0.041	⋯	⋯	⋯	LOTIS
2015 Dec 03.63	360.13	137.16	⋯	18.713 ± 0.063	⋯	⋯	⋯	⋯	⋯	LCO
2015 Dec 06.84	363.34	140.28	19.211 ± 0.100	18.886 ± 0.041	⋯	⋯	⋯	18.707 ± 0.037	18.852 ± 0.081	LCO
2015 Dec 07.33	363.83	140.76	⋯	18.778 ± 0.105	18.790 ± 0.103	⋯	⋯	⋯	⋯	LOTIS
2015 Dec 09.64	366.14	143.00	⋯	18.759 ± 0.104	⋯	⋯	⋯	⋯	⋯	LCO
2015 Dec 10.33	366.83	143.67	⋯	19.002 ± 0.051	18.877 ± 0.047	18.277 ± 0.066	⋯	⋯	⋯	LOTIS
2015 Dec 13.98	370.48	147.23	19.579 ± 0.122	19.106 ± 0.066	⋯	⋯	⋯	18.899 ± 0.056	⋯	LCO
2015 Dec 16.33	372.83	149.51	⋯	19.255 ± 0.063	19.029 ± 0.033	18.587 ± 0.099	⋯	⋯	⋯	LOTIS
2015 Dec 18.01	374.51	151.14	19.621 ± 0.042	19.346 ± 0.043	⋯	⋯	19.362 ± 0.020	19.008 ± 0.035	⋯	Coper
2015 Dec 18.28	374.78	151.40	⋯	19.243 ± 0.048	⋯	⋯	⋯	19.075 ± 0.046	⋯	LCO
2015 Dec 18.90	375.40	152.01	⋯	19.217 ± 0.024	⋯	⋯	19.388 ± 0.021	19.033 ± 0.020	19.378 ± 0.027	Coper
2015 Dec 19.33	375.83	152.43	⋯	19.349 ± 0.068	19.188 ± 0.076	⋯	⋯	⋯	⋯	LOTIS
2015 Dec 23.86	380.36	156.83	⋯	19.225 ± 0.180	⋯	⋯	⋯	19.253 ± 0.214	⋯	LCO
2015 Dec 27.88	384.38	160.74	19.815 ± 0.041	19.445 ± 0.036	⋯	⋯	⋯	19.198 ± 0.028	19.495 ± 0.039	LT
2015 Dec 28.21	384.71	161.06	20.114 ± 0.186	19.464 ± 0.049	⋯	⋯	⋯	19.189 ± 0.041	19.446 ± 0.084	LCO
2015 Dec 30.24	386.74	163.04	⋯	19.528 ± 0.213	⋯	⋯	⋯	19.177 ± 0.099	19.368 ± 0.107	LCO
2016 Jan 01.27	388.77	165.01	⋯	19.630 ± 0.048	19.440 ± 0.047	19.046 ± 0.080	⋯	⋯	⋯	LOTIS
2016 Jan 03.27	390.77	166.96	⋯	19.833 ± 0.146	19.475 ± 0.097	18.889 ± 0.088	⋯	⋯	⋯	LOTIS
2016 Jan 05.92	393.42	169.53	20.198 ± 0.021	19.573 ± 0.018	⋯	⋯	⋯	19.391 ± 0.016	19.601 ± 0.022	LT
2016 Jan 10.94	398.44	174.41	20.347 ± 0.017	19.719 ± 0.017	⋯	⋯	⋯	19.574 ± 0.013	19.761 ± 0.025	LT
2016 Jan 12.27	399.77	175.71	⋯	19.876 ± 0.145	⋯	⋯	⋯	⋯	⋯	LOTIS
2016 Jan 16.90	404.40	180.21	20.487 ± 0.051	19.842 ± 0.042	⋯	⋯	⋯	19.697 ± 0.028	⋯	LT
2016 Jan 18.20	405.70	181.48	⋯	19.743 ± 0.147	19.633 ± 0.089	⋯	⋯	⋯	⋯	LOTIS
2016 Jan 21.87	409.37	185.05	20.546 ± 0.107	⋯	⋯	⋯	⋯	⋯	⋯	LT
2016 Jan 26.89	414.39	189.93	20.783 ± 0.016	20.192 ± 0.018	⋯	⋯	⋯	20.038 ± 0.014	20.242 ± 0.027	LT
2016 Jan 27.13	414.63	190.16	⋯	20.187 ± 0.155	19.931 ± 0.076	19.464 ± 0.115	⋯	⋯	⋯	LOTIS
2016 Jan 30.13	417.63	193.08	⋯	20.244 ± 0.095	20.226 ± 0.085	19.748 ± 0.120	⋯	⋯	⋯	LOTIS
2016 Feb 05.13	423.63	198.91	⋯	20.320 ± 0.186	⋯	⋯	⋯	⋯	⋯	LOTIS
2016 Feb 08.13	426.63	201.83	⋯	20.478 ± 0.149	⋯	19.784 ± 0.213	⋯	⋯	⋯	LOTIS
2016 Feb 11.10	429.60	204.72	⋯	20.468 ± 0.117	20.523 ± 0.102	⋯	⋯	⋯	⋯	LOTIS
2016 Feb 24.13	442.63	217.39	⋯	20.729 ± 0.049	⋯	⋯	⋯	⋯	⋯	MDM
2016 Feb 25.12	443.62	218.36	⋯	20.625 ± 0.030	⋯	⋯	⋯	⋯	⋯	MDM
2016 Mar 03.85	451.35	225.87	⋯	⋯	⋯	⋯	⋯	20.768 ± 0.082	⋯	LT

Table 1
(Continued)

UT Date	JD-2457,000	Phase[a] (days)	*B* (mag)	*V* (mag)	*R* (mag)	*I* (mag)	*g* (mag)	*r* (mag)	*i* (mag)	Telescope[b] /Inst.
2016 Mar 04.85	452.35	226.85	⋯	⋯	⋯	⋯	⋯	20.819 ± 0.094	⋯	LT
2016 Mar 09.87	457.37	231.73	⋯	20.924 ± 0.045	⋯	⋯	⋯	⋯	⋯	LT
2016 Mar 12.10	459.60	233.90	⋯	21.182 ± 0.022	⋯	⋯	⋯	⋯	⋯	Mag
2016 Mar 15.88	463.38	237.58	⋯	21.213 ± 0.029	⋯	⋯	21.598 ± 0.049	21.163 ± 0.033	20.977 ± 0.033	LT, NOT
2016 Apr 09.99	488.49	261.99	22.290 ± 0.060	21.709 ± 0.049	⋯	⋯	⋯	21.491 ± 0.028	21.317 ± 0.043	Mag

Notes. Data observed within 5 hr are represented under a single-epoch observation.
[a] Rest-frame days with reference to the explosion epoch JD 2457219.10.
[b] The abbreviations of telescope/instrument used are as follows: ASASSN—ASAS-SN quadruple 14 cm telescopes; LCO—Las Cumbres Observatory 1 m telescope network; LT—2 m Liverpool Telescope; NOT—ALFOSC mounted on 2.0 m NOT telescope; MDM—2.4 m MDM telescope; LOTIS—0.6 m Super-Lotis telescope; TJO—0.8 m TJO telescope; Coper—1.8 m Copernico telescope; Mag—IMACS mounted on 6.5 m *Magellan* Baade telescope.

Table 2
Summary of Spectroscopic Observations of ASASSN-15nx

UT Date (yy mm dd.dd)	JD 2457000+	Phase[a] (days)	Telescope[b]
2015 Sep 08.12	273.62	53.0	Coper
2015 Sep 08.38	273.88	53.3	Dup
2015 Oct 13.46	308.96	87.4	MOD
2015 Oct 22.00	318.50	96.7	Coper
2015 Oct 23.50	319.00	97.2	Bok
2015 Nov 05.09	331.59	109.4	NOT
2015 Nov 05.10	331.60	109.4	Coper
2015 Nov 16.99	343.49	121.0	Coper
2015 Nov 18.98	345.48	122.9	Coper
2015 Nov 19.30	345.80	123.2	Bok
2015 Dec 01.32	357.82	134.9	MMT
2015 Dec 02.97	359.47	136.5	Coper
2015 Dec 07.25	363.75	140.7	MOD
2015 Dec 17.96	374.46	151.1	Coper
2016 Jan 02.21	389.71	165.9	MOD
2016 Jan 02.29	389.79	166.0	Bok
2016 Jan 16.08	403.58	179.4	MagE
2016 Mar 12.09	459.59	233.9	IMAC
2016 Apr 10.01	488.51	262.0	IMAC

Notes.
[a] The phase is the number of rest-frame days after the adopted explosion epoch JD 2457219.10
[b] The telescope abbreviations are—Coper : Copernico telescope; Dup : du Pont telescope; MOD: MODS spectrograph on LBT; Bok: Bok telescope; MMT: MMT Observatory; NOT: Nordic Optical Telescope; MagE: Echellette Spectrograph on *Magellan* Baade telescope; IMAC: IMACS spectrograph on *Magellan* Baade telescope.

Table 3
Blackbody Bolometric Luminosity

Phase[a] (days)	Luminosity ($Log_{10}[L$ erg s^{-1}])	Phase[a] (days)	Luminosity ($\mathrm{Log}_{10}[L$ erg s^{-1}])
3.72	43.49 ± 0.17	118.38	42.46 ± 0.40
5.65	43.53 ± 0.17	121.02	42.44 ± 0.13
7.59	43.56 ± 0.17	121.30	42.45 ± 0.13
23.37	43.48 ± 0.17	122.94	42.43 ± 0.11
24.44	43.50 ± 0.20	124.21	42.40 ± 0.12
27.10	43.47 ± 0.17	126.01	42.40 ± 0.89
28.20	43.45 ± 0.16	127.13	42.38 ± 0.63
29.72	43.44 ± 0.14	131.02	42.35 ± 0.24
31.82	43.38 ± 0.16	131.70	42.34 ± 0.23
32.63	43.38 ± 0.15	132.97	42.32 ± 0.25
35.71	43.32 ± 0.15	133.16	42.31 ± 0.17
37.65	43.28 ± 0.13	134.12	42.33 ± 0.17
38.63	43.27 ± 0.11	135.30	42.31 ± 0.17
41.61	43.23 ± 0.11	135.52	42.31 ± 0.14
44.44	43.21 ± 0.12	136.34	42.30 ± 0.13
47.34	43.16 ± 0.10	136.56	42.30 ± 0.13
49.66	43.15 ± 0.10	136.87	42.28 ± 0.19
56.14	43.06 ± 0.21	137.16	42.31 ± 0.14
61.98	43.00 ± 0.10	140.28	42.29 ± 0.25
63.02	42.99 ± 0.10	140.76	42.28 ± 0.21
64.56	42.97 ± 0.16	143.00	42.27 ± 0.19
67.12	42.96 ± 0.21	143.67	42.23 ± 0.19
70.64	42.90 ± 0.15	147.22	42.17 ± 0.24
72.94	42.89 ± 0.22	149.51	42.14 ± 0.18
76.66	42.84 ± 0.19	151.14	42.12 ± 0.19
77.63	42.82 ± 0.21	151.41	42.12 ± 0.16
85.57	42.78 ± 0.15	152.01	42.12 ± 0.17
86.10	42.76 ± 0.16	152.43	42.10 ± 0.17
89.58	42.72 ± 0.16	156.83	42.09 ± 0.20
94.77	42.69 ± 0.18	160.74	42.05 ± 0.16
96.74	42.68 ± 0.08	161.12	42.00 ± 0.25
99.47	42.65 ± 0.16	165.01	41.96 ± 0.37
102.90	42.62 ± 0.16	166.96	41.93 ± 0.24
105.52	42.63 ± 0.10	169.53	41.95 ± 0.12
107.23	42.60 ± 0.15	174.42	41.90 ± 0.10
109.48	42.54 ± 0.11	175.71	41.86 ± 0.16
111.34	42.55 ± 0.08	180.21	41.85 ± 0.15
111.57	42.51 ± 0.16	181.48	41.86 ± 0.15
111.60	42.52 ± 0.18	185.05	41.80 ± 0.23
112.30	42.55 ± 0.08	187.31	41.76 ± 0.20
112.54	42.50 ± 0.12	189.93	41.72 ± 0.13
113.25	42.53 ± 0.08	190.16	41.73 ± 0.16
113.52	42.49 ± 0.12	193.08	41.68 ± 0.14
114.24	42.54 ± 0.11	194.79	41.68 ± 0.13
115.46	42.48 ± 0.11	195.74	41.67 ± 0.14
116.19	42.50 ± 0.09	198.91	41.65 ± 0.22
117.14	42.49 ± 0.09	201.83	41.61 ± 0.27
117.39	42.49 ± 0.29	261.99	41.32 ± 0.26

Notes. The bolometric luminosity is calculated by fitting the blackbody on *BVI*-band photometric data. During pre-peak phases ($\lesssim$23.37 day), where only *V*-band data are available, the blackbody temperature is extrapolated and luminosity is calculated after scaling the blackbody SED to match *V*-band data, taking the broadband filter response into account as well. At 261.99 days, the fitting is done on *BVri*-band data.
[a] Rest-frame days relative to the adopted explosion epoch JD 2457219.10.

ORCID iDs

Subhash Bose https://orcid.org/0000-0003-3529-3854
Subo Dong https://orcid.org/0000-0002-1027-0990
C. S. Kochanek https://orcid.org/0000-0001-6017-2961
David Bersier https://orcid.org/0000-0001-7485-3020
J. L. Prieto https://orcid.org/0000-0003-0943-0026
Juna Kollmeier https://orcid.org/0000-0001-9852-1610
E. Cappellaro https://orcid.org/0000-0001-5008-8619
Peter Milne https://orcid.org/0000-0002-0370-157X
Leonardo Tartaglia https://orcid.org/0000-0003-3433-1492
Charles D. Kilpatrick https://orcid.org/0000-0002-5740-7747
Barry F. Madore https://orcid.org/0000-0002-1576-1676
Jeffrey A. Rich https://orcid.org/0000-0002-5807-5078

References

Anderson, J. P., González-Gaitán, S., Hamuy, M., et al. 2014, ApJ, 786, 67
Arcavi, I., Gal-Yam, A., Cenko, S. B., et al. 2012, ApJL, 756, L30
Arcavi, I., Wolf, W. M., Howell, D. A., et al. 2016, ApJ, 819, 35
Arnett, W. D. 1980, ApJ, 237, 541
Arnett, W. D., & Fu, A. 1989, ApJ, 340, 396
Astropy Collaboration, Robitaille, T. P., Tollerud, E. J., et al. 2013, A&A, 558, A33
Barbon, R., Ciatti, F., & Rosino, L. 1979, A&A, 72, 287
Barbon, R., Ciatti, F., & Rosino, L. 1982a, A&A, 116, 35
Barbon, R., Ciatti, F., Rosino, L., Ortolani, S., & Rafanelli, P. 1982b, A&A, 116, 43
Barnsley, R. M., Smith, R. J., & Steele, I. A. 2012, AN, 333, 101
Benetti, S., Zampieri, L., Pastorello, A., et al. 2018, MNRAS, 476, 261
Bersten, M. C., & Hamuy, M. 2009, ApJ, 701, 200
Blinnikov, S. I., & Bartunov, O. S. 1993, A&A, 273, 106

Bose, S., Dong, S., Pastorello, A., et al. 2018, ApJ, 853, 57
Bose, S., Kumar, B., Misra, K., et al. 2016, MNRAS, 455, 2712
Bose, S., Kumar, B., Sutaria, F., et al. 2013, MNRAS, 433, 1871
Bose, S., Sutaria, F., Kumar, B., et al. 2015a, ApJ, 806, 160
Bose, S., Valenti, S., Misra, K., et al. 2015b, MNRAS, 450, 2373
Branch, D., Benetti, S., Kasen, D., et al. 2002, ApJ, 566, 1005
Branch, D., Falk, S. W., Uomoto, A. K., et al. 1981, ApJ, 244, 780
Brown, T. M., Baliber, N., Bianco, F. B., et al. 2013, PASP, 125, 1031
Cardelli, J. A., Clayton, G. C., & Mathis, J. S. 1989, ApJ, 345, 245
Chatzopoulos, E., Wheeler, J. C., & Vinko, J. 2012, ApJ, 746, 121
Chugai, N. N. 2006, AstL, 32, 739
Chugai, N. N. 2009, MNRAS, 400, 866
Chugai, N. N., Chevalier, R. A., & Utrobin, V. P. 2007, ApJ, 662, 1136
Clocchiatti, A., & Wheeler, J. C. 1997, ApJ, 491, 375
de Vaucouleurs, G., de Vaucouleurs, A., Buta, R., Ables, H. D., & Hewitt, A. V. 1981, PASP, 93, 36
Doggett, J. B., & Branch, D. 1985, AJ, 90, 2303
Dong, S., Shappee, B. J., Prieto, J. L., et al. 2016, Sci, 351, 257
Elias-Rosa, N., Cappellaro, E., Benetti, S., et al. 2015, ATel, 8016
Elmhamdi, A., Danziger, I. J., Chugai, N., et al. 2003, MNRAS, 338, 939
Faran, T., Poznanski, D., Filippenko, A. V., et al. 2014, MNRAS, 445, 554
Fassia, A., Meikle, W. P. S., Chugai, N., et al. 2001, MNRAS, 325, 907
Filippenko, A. V. 1997, ARA&A, 35, 309
Fisher, A., Branch, D., Hatano, K., & Baron, E. 1999, MNRAS, 304, 67
Fisher, A., Branch, D., Nugent, P., & Baron, E. 1997, ApJL, 481, L89
Gal-Yam, A. 2012, Sci, 337, 927
Gutiérrez, C. P., Anderson, J. P., Hamuy, M., et al. 2014, ApJL, 786, L15
Gutiérrez, C. P., Anderson, J. P., Hamuy, M., et al. 2017, ApJ, 850, 89
Hamuy, M. 2003, ApJ, 582, 905
Hamuy, M., Pinto, P. A., Maza, J., et al. 2001, ApJ, 558, 615
Hamuy, M., & Suntzeff, N. B. 1990, AJ, 99, 1146
Henden, A. A., Templeton, M., Terrell, D., et al. 2016, yCat, 2336
Höflich, P., Wheeler, J. C., & Wang, L. 1999, ApJ, 521, 179
Holoien, T. W.-S., Brown, J. S., Stanek, K. Z., et al. 2017a, MNRAS, 467, 1098
Holoien, T. W.-S., Brown, J. S., Stanek, K. Z., et al. 2017b, MNRAS, 471, 4966
Holoien, T. W.-S., Kochanek, C. S., Prieto, J. L., et al. 2016a, MNRAS, 455, 2918
Holoien, T. W.-S., Prieto, J. L., Pejcha, O., et al. 2016b, AcA, 66, 219
Holoien, T. W.-S., Stanek, K. Z., Kochanek, C. S., et al. 2017c, MNRAS, 464, 2672
Inserra, C., Turatto, M., Pastorello, A., et al. 2012, MNRAS, 422, 1122
Jeffery, D. J. 1999, arXiv:astro-ph/9907015
Kasen, D., Woosley, S. E., & Heger, A. 2011, ApJ, 734, 102
Katz, B., Kushnir, D., & Dong, S. 2013, arXiv:1301.6766
Kiyota, S., Holoien, T. W.-S., Stanek, K. Z., et al. 2015, ATel, 7895
Kushnir, D. 2015a, arXiv:1506.02655
Kushnir, D. 2015b, arXiv:1502.03111
Kushnir, D., & Katz, B. 2015, ApJ, 811, 97
Leonard, D. C., Filippenko, A. V., Barth, A. J., & Matheson, T. 2000, ApJ, 536, 239
Leonard, D. C., Filippenko, A. V., Gates, E. L., et al. 2002, PASP, 114, 35
Li, W., Chornock, R., Leaman, J., et al. 2011a, MNRAS, 412, 1473
Li, W., Leaman, J., Chornock, R., et al. 2011b, MNRAS, 412, 1441
Lupton, R. H., Jurić, M., Ivezić, Z., et al. 2005, BAAS, 37, 1384
Müller, T., Prieto, J. L., Pejcha, O., & Clocchiatti, A. 2017, ApJ, 841, 127
Munari, U., Henden, A., Belligoli, R., et al. 2013, New A, 20, 30
Nakar, E., Poznanski, D., & Katz, B. 2016, ApJ, 823, 127
Pejcha, O., & Prieto, J. L. 2015, ApJ, 806, 225
Piascik, A. S., Steele, I. A., Bates, S. D., et al. 2014, Proc. SPIE, 9147, 91478H
Planck Collaboration, Ade, P. A. R., Aghanim, N., et al. 2016, A&A, 594, A13
Prajs, S., Sullivan, M., Smith, M., et al. 2017, MNRAS, 464, 3568
Quimby, R. M., Aldering, G., Wheeler, J. C., et al. 2007, ApJL, 668, L99
Rabinak, I., & Waxman, E. 2011, ApJ, 728, 63
Rest, A., Foley, R. J., Gezari, S., et al. 2011, ApJ, 729, 88
Sahu, D. K., Anupama, G. C., Srividya, S., & Muneer, S. 2006, MNRAS, 372, 1315
Schlafly, E. F., & Finkbeiner, D. P. 2011, ApJ, 737, 103
Schlegel, E. M. 1990, MNRAS, 244, 269
Shappee, B. J., Prieto, J. L., Grupe, D., et al. 2014, ApJ, 788, 48
Smith, N., Cenko, S. B., Butler, N., et al. 2012a, MNRAS, 420, 1135
Smith, N., Chornock, R., Li, W., et al. 2008a, ApJ, 686, 467
Smith, N., Foley, R. J., & Filippenko, A. V. 2008b, ApJ, 680, 568
Smith, N., Li, W., Foley, R. J., et al. 2007, ApJ, 666, 1116
Smith, N., Mauerhan, J. C., Silverman, J. M., et al. 2012b, MNRAS, 426, 1905
Smith, N., Silverman, J. M., Chornock, R., et al. 2009, ApJ, 695, 1334
Spiro, S., Pastorello, A., Pumo, M. L., et al. 2014, MNRAS, 439, 2873
Stetson, P. B. 1987, PASP, 99, 191
Swartz, D. A., Sutherland, P. G., & Harkness, R. P. 1995, ApJ, 446, 766
Taubenberger, S., Kromer, M., Pakmor, R., et al. 2013, ApJL, 775, L43
Taubenberger, S., Valenti, S., Benetti, S., et al. 2009, MNRAS, 397, 677
Terreran, G., Jerkstrand, A., Benetti, S., et al. 2016, MNRAS, 462, 137
Tody, D. 1993, in ASP Conf. Ser. 52, Astronomical Data Analysis Software and Systems II, ed. R. J. Hanisch, R. J. V. Brissenden, & J. Barnes (San Francisco, CA: ASP), 173
Tomasella, L., Cappellaro, E., Fraser, M., et al. 2013, MNRAS, 434, 1636
Utrobin, V. P., Chugai, N. N., & Andronova, A. A. 1995, A&A, 295, 129
Valenti, S., Howell, D. A., Stritzinger, M. D., et al. 2016, MNRAS, 459, 3939
Valenti, S., Sand, D., Stritzinger, M., et al. 2015, MNRAS, 448, 2608
Valenti, S., Taubenberger, S., Pastorello, A., et al. 2012, ApJL, 749, L28
Wang, L., Howell, D. A., Höflich, P., & Wheeler, J. C. 2001, ApJ, 550, 1030
Wheeler, J. C., Harkness, R. P., & Cappellaro, E. 1987, in 13th Texas Symp. Relativistic Astrophysics, ed. M. P. Ulmer (Teaneck, NJ: World Scientific), 402
Wygoda, N., Elbaz, Y., & Katz, B. 2017, arXiv:1711.00969
Young, T. R., & Branch, D. 1989, ApJL, 342, L79